Modeling Hydrodynamics of Gas–Liquid Airlift Reactor

Samuel Talvy, Arnaud Cockx, Alain Liné
Laboratoire d'Ingénierie des Systèmes Biologiques et des Procédés (UMR INSA-CNRS 5504, UMR INSA-INRA 792), 31077 Toulouse cedex, France

DOI 10.1002/aic.11078
Published online January 4, 2007 in Wiley InterScience (www.interscience.wiley.com).

This article deals with the physical modeling and numerical simulation of two-phase bubbly flow in an airlift internal loop reactor. The objective is to show the ability of computational fluid dynamics (CFD) to correctly simulate hydrodynamics and axial dispersion in such a bubbly reactor. The modeling of two-phase bubbly flow is based on the so-called two-fluid model derived from Reynolds-averaged Navier–Stokes equations in two-phase flow. From the local perspective, CFD leads to the distributions of phases, interfacial area, and velocity field in the whole volume of the airlift. Numerical simulations are discussed after comparison with experimental data. Sensitivity analysis is then presented to highlight the main parameters that must be taken into account in two-fluid modeling, especially in terms of interfacial transfer of momentum and turbulence. Once local hydrodynamics has been discussed and validated, the axial dispersion is then addressed. The axial dispersion coefficient is estimated from simulation of transport equation of salt concentration. Given the time evolution of the concentration, measured by a "numerical" probe located in computed airlift reactor, it is possible to numerically estimate the axial dispersion in the airlift, in the same way as in the experiments. The axial dispersion coefficient determined after simulation is compared with the experimental one and the ability of CFD to simulate mixing time and axial dispersion is shown. In addition, a physical analysis of axial dispersion is proposed.
 AIChE J, 53: 335–353, 2007
Keywords: airlift, hydrodynamics, two-fluid model, mixing, axial dispersion, turbulence, computational fluid dynamics (CFD)

Introduction

This study focuses primarily on associating the fluid mechanics approach with that of the chemical engineering approach. The fluid mechanics approach usually concentrates efforts on solving local Reynolds equations by developing closure models on interfacial transfer and/or turbulence; it is generally applied to basic flow problems in simplified geometry. At the same time, the chemical engineering approach usually concentrates efforts on overall studies, leading to global laws that are very useful for industrial problems.

In chemical engineering, hydrodynamics of airlift reactor is classically analyzed in terms of axial dispersion. To better understand the meaning of axial dispersion, and then to improve its determination, the use of computational fluid dynamics (CFD) is actually helpful. Basically, CFD enables one to perform the same experiment on a computed pilot than on a laboratory pilot. For example, in this article, we will use a numerical tracer and a numerical probe to determine mixing time and axial dispersion. Indeed, this numerical experiment sets out to first correctly simulate the local two-phase flow hydrodynamics and, in a second step, to sim-

Correspondence concerning this article should be addressed to A. Liné at alain.line@insa-toulouse.fr.

ulate the transport of concentration. As soon as these simulations are validated by comparison to experiments, the distribution of the two phases can be considered as reliable. Then, given a correct local distribution of interfacial area and associated hydrodynamics, local mass transfer can be locally simulated. Mass transfer will be presented and discussed in a companion article. One of the goals of this first article is to emphasize the most important phenomenon to be modeled in airlift reactor, among the numerous phenomena involved in turbulent two-phase bubbly flow.

In fact, many different CFD codes are now available; we have chosen to use one of the existing codes (Fluent®, Fluent Inc., Lebanon, NH). Given this code, it is possible to focus our research on the physical phenomena and to test different physical modeling of gas–liquid interactions. In Fluent® code, the two-fluid model can be used in a Eulerian–Eulerian approach. Our goal is to better understand the closure laws and to determine the main parameters in bubbly flow in an airlift reactor.

Airlifts have been mainly reviewed in the domain of bioreactors.[1–4] In the last review, Merchuk[4] mentioned only two works based on CFD in airlift reactors: Cockx et al.[5] and Mudde and van den Akker.[6] In Cockx et al.,[5] ASTRID code was used. It was the first attempt at modeling bubbly flow in an airlift reactor with a local two-fluid model approach. However, the closure relations on momentum and turbulence interfacial transfers were not analyzed in detail and need to be better understood. Mudde and van den Akker[6] used a model very similar to that of Cockx et al.[5] Unfortunately, the validation of their model is limited to global gas fraction. Since this date, van Baten et al.[7] and Oey et al.[8] presented CFD works to describe hydrodynamics of internal airlift reactors. The simulations of van Baten et al.[7] are based on CFX code. In the Eulerian approach, the authors model the interfacial transfer of momentum in terms of drag, without added mass effect. The drag coefficient is constant and related to the Eötvös number, following the modeling of Clift et al.[9] Gas bubble dispersion related to drift velocity is not taken into account in drag modeling. Nothing is said about the interfacial transfer of turbulent kinetic energy or its dissipation rate. The authors obtain a good agreement between simulations and experiments, in terms of global gas holdup in the riser and downcomer and in terms of global liquid circulation.

However, no comparison to experiments is proposed in terms of local data such as longitudinal or horizontal distributions of gas fraction or liquid velocity. In consequence, the local modeling cannot be validated. In particular, the role of dispersion related to drift velocity cannot be analyzed. Oey et al.[8] present numerical simulations of an oscillating internal-loop airlift reactor. Three-dimensional (3D) simulations are performed in a Eulerian two-fluid approach. The interfacial term of transfer is taken into account in the modeling of the turbulence in the liquid phase. The authors model the interfacial transfer of momentum in terms of drag, including added mass effect. The drag coefficient is modeled by the Schiller and Naumann[10] correlation, which is more adapted to solid particles than to gas bubbles. The drift velocity is not taken into account in the drag modeling. The authors focus on transient phenomena and compare the predicted period of oscillations in the downcomer to experimental values. The transient behavior is probably related to the modeling of the added mass.[11,12] Unfortunately, the simulations are not compared to experimental data in terms of local or global gas fraction or liquid velocity. In conclusion, the existing works on CFD applied to airlift reactor are scarce. In addition, local data are rarely used to validate simulations. The lack of references to local data limits the analysis of closure relations used in CFD works.

In the present article, we will refer to experimental data acquired by Couvert[13] on longitudinal and horizontal profiles of gas fraction in the riser and in the downcomer of an airlift reactor. We will also use data on velocity profile in the downcomer.[14]

In the first section of the article, the two-fluid model equations are recalled and specific closure relations are analyzed. With the numerical results being compared to experiments acquired on laboratory pilot, the experimental facility (airlift reactor) and the numerical code are presented in the second section. In the third section, the study focuses on validation of bubbly flow simulations. The objective is to correctly predict longitudinal profiles of gas fraction in the riser and the downcomer and velocity profile in the downcomer, guided by the aim of attaining a solid understanding of local hydrodynamics parameters such as characteristic scale of bubbles and interfacial momentum transfer coefficients (drag, added mass). In section four, complementary numerical results are presented to analyze the sensitivity of the computed results to physical parameters such as gas dispersion (drift velocity), free surface deformation, and interfacial momentum transfer coefficients (drag, added mass). In the present study, the bubble diameter is imposed from experimental observations. Once two-fluid modeling has been validated and analyzed, axial dispersion and mixing time are addressed.

Very few articles have been devoted to the simulation of axial dispersion in bubbly reactors. van Baten and Krishna[15] presented such simulations in a bubble column. The authors obtained good predictions and concluded on the efficiency of CFD code for scale-up design of reactors. The present article presents the simulation of axial dispersion in an airlift reactor. In the fifth section, the transport of salt concentration is simulated in the liquid phase. The simulation of concentration is validated by comparison with experiments, in terms of axial dispersion and mixing time. The respective contributions of turbulent diffusion and spatial dispersion to the axial dispersion are analyzed and discussed.

The objective of the article is definitely not to fit the experimental data "exactly," by adjusting different coefficients of the model. The aim is first to select the most important parameters controlling hydrodynamics and axial dispersion and then to estimate the efficiency of the available closure relations to sufficiently (or insufficiently) predict the experiments. In consequence, only three gas flow rates were used to validate the model and only one gas flow rate is studied in terms of sensitivity analysis of the modeling to the aforementioned parameters. In addition, as pointed out by Merchuk et al.,[16] axial fluid mixing has been extensively studied in bubble columns, although there are very few studies in the literature addressing gas holdup, liquid velocity, and axial mixing in airlift reactors. The present study can contribute to such local analysis of gas–liquid airlift reactors.

Mathematical Modeling

The development of the Eulerian two-fluid model is now classical. Consequently, the basic equations driving two-phase flow hydrodynamics will be briefly recalled. The flow is assumed to be isothermal.

Mass balance

The mass balance is given by

$$\frac{\partial \alpha_k \rho_k}{\partial t} + \nabla \alpha_k \rho_k \overline{U_k} = \overline{m_k} \tag{1}$$

where α_k is the volume fraction, index k stands for gas (G) or liquid (L), ρ_k (kg m^{-3}) is the phase density, and $\overline{U_k}$ (m s^{-1}) is the local, statistical averaged velocity associated with phase k. On the right-hand side appears a term that represents the statistical averaged interfacial mass transfer. In the present work, the interfacial mass transfer will be neglected.

Momentum balance

The momentum equation for phase k is given by

$$\frac{\partial}{\partial t}(\alpha_k \rho_k \overline{U_k}) + \nabla \alpha_k \rho_k \overline{U_k U_k} = \alpha_k \rho_k B_k - \nabla \alpha_k P_k + \nabla \alpha_k (\overline{\tau_k} - \rho_k \overline{u_k' u_k'}) + \overline{u_k m_k} + \overline{M_k} \tag{2}$$

where B_k (m s^{-2}) is the gravitational acceleration, P_k (kg m^{-1} s^{-2}) is the pressure in phase k, $\overline{u_k' u_k'}$, (m^2 s^{-2}) is the phase Reynolds stress tensor, and $\overline{M_k}$ (kg m^{-2} s^{-2}) is the interfacial transfer of momentum arising from pressure and viscous stress distributions over the gas–liquid interface. Equation 2 can be rewritten as follows:

$$\frac{\partial}{\partial t}(\alpha_k \rho_k \overline{U_k}) + \nabla \cdot \alpha_k \rho_k \overline{U_k U_k} = \alpha_k \rho_k g - \alpha_k \nabla \overline{P_k} + \nabla \cdot \alpha_k (\overline{\tau_k} - \rho_k \overline{u_k' u_k'}) + \overline{u_k m_k} + \overline{I_k} \tag{3}$$

where I_k represents the interfacial momentum transfer that results after substracting the average pressure. It can be expressed as[17]

$$\overline{I_G} = -\overline{I_L} = a_p \frac{1}{2} \rho_L C_D |\overline{V_r}| \overline{V_r} + \alpha_G \rho_L C_A \left[\frac{\partial \overline{U_r}}{\partial t} + \overline{U_G} \cdot \nabla \overline{U_r} \right] + \nabla [\alpha_G \rho_L C_A \overline{u_G' u_r'}] - \rho_L \overline{u_G' u_L'} \cdot \nabla \alpha_G \tag{4}$$

The first term on the right-hand side of Eq. 4 accounts for drag, which will be discussed below. The second and third terms account for added mass effects. The last term accounts for turbulent pressure.[18] The last term was developed in the frame of homogeneous turbulence. Because the circulation in the airlift is controlled by the gas flow, and primarily by buoyancy effects, we will focus on drag and added mass mechanisms. In the momentum equation of the two-fluid model, the interfacial transfer of momentum related to drag is expressed as

$$\overline{I_{DG}} = -\overline{I_{DL}} = a_p \frac{1}{2} \rho_L C_D |\overline{V_r}| \overline{V_r}$$

In this drag term, appears the relative velocity $\overline{V_r}$ and the drag coefficient C_D. In the case of spherical bubbles, the projected interfacial area a_p is given by $a_p = (3/4)(\alpha_G / r_b)$, where r_b is the bubble radius; thus

$$\overline{I_{DG}} = \alpha_G \rho_L \frac{3 C_D}{8 r_b} |\overline{V_r}| \overline{V_r} \tag{5}$$

The radius r_b corresponds to the radius of the sphere of volume equivalent to that of the distorted bubble. The drag coefficient used in the present work was proposed by Karamanev and Nikolov,[19] and is expressed as

$$C_D = \frac{24}{\mathrm{Re}}(1 + 0.15\mathrm{Re}^{0.687}) + \frac{0.413}{1 + 16.3\mathrm{Re}^{-1.09}} \quad \text{for} \quad \mathrm{Re} < 135 \tag{6}$$

$$C_D = 0.95 \quad \text{for} \quad \mathrm{Re} > 135 \tag{7}$$

This expression is close to Schiller and Naumann[10] correlation, for low bubble Reynolds number. The bubble Reynolds number is defined as

$$\mathrm{Re} = \frac{\rho_L d_b |\overline{V_r}|}{\mu_L} \tag{8}$$

In two-phase flow, it is classical to refer to $\overline{U_r}$, the difference of velocity between the two phases:

$$\overline{U_r} = \overline{U_G} - \overline{U_L} \tag{9}$$

However, the relative velocity $\overline{V_r}$ is not equal to the difference of velocity of the two phases. Following Simonin's proposal, it is defined as

$$\overline{V_r} = \overline{U_G} - \overline{U_L} - \overline{v_d} \tag{10}$$

The relative velocity $\overline{V_r}$ is the statistical average of the local instantaneous relative velocity between each bubble and the surrounding liquid. In other words, it represents the statistical average of relative velocity of the liquid seen by the gas. The statistical average of the turbulent fluctuating liquid velocity in the liquid is equal to zero, but the statistical average of the turbulent fluctuating liquid velocity seen by the gas is not equal to zero. Therefore, on the right-hand side of the previous equation, an additional term, $\overline{v_d}$, appears, called drift velocity, arising from the correlation between instantaneous distributions of bubbles and large scale liquid motions. This term needs to be analyzed in detail. The modeling of the drift velocity used in this article is attributed to Simonin and Viollet:[20]

$$\overline{v_d} = -D_{GL}^t \left[\frac{1}{\alpha_G} \nabla \alpha_G - \frac{1}{\alpha_L} \nabla \alpha_L \right] \tag{11}$$

where the fluid-bubble turbulent dispersion term D_{GL}^t is related to the turbulence characteristic scales. The significant role of the drift velocity will be shown later in the discussion. It is thus necessary to detail its modeling. In the case of quasi fully developed upward cocurrent bubbly flow, the vertical component of the drift velocity $\overline{v_d}$ is negligible compared to the longitudinal (vertical) relative velocity $\overline{U_r}$. Consequently, in the longitudinal equation of momentum, the drift velocity could be neglected. The norm of the relative velocity could also be simplified, given that $|\overline{V_r}| \approx |\overline{U_r}|$. However, as we will see in the discussion, the role of the drift velocity in the horizontal component of momentum balance equation is significant and necessary to explain the dispersion of the bubbles.

The fluid-bubble turbulent dispersion term is modeled as

$$D_{GL}^t = \frac{1}{3} \tau_{GL}^t \overline{u_G' u_L'} \tag{12}$$

where τ_{GL}^t is the characteristic timescale of the turbulence seen by the gas phase. This characteristic timescale is related

to the characteristic time of the turbulence scale in the liquid phase, τ_L^t, classically expressed in terms of turbulent kinetic energy and dissipation rate by

$$\tau_L^t = \frac{3}{2} C_\mu \frac{k_L}{\varepsilon_L} \tag{13}$$

τ_{GL}^t is expressed by

$$\tau_{GL}^t = \frac{\tau_L^t}{\sigma_{kL}} \left(1 + C_\beta \zeta_r^2\right)^{-t/2} \tag{14}$$

where ζ_r is the ratio of the characteristic time of the turbulence in the liquid and the characteristic timescale of the bubble necessary to cross the containing energy eddies:

$$\zeta_r = \frac{|\overline{V_r}|}{\sqrt{2k_L/3}} \tag{15}$$

The link between the characteristic timescale of the turbulence seen by the gas phase, τ_{GL}^t, and the characteristic time of the turbulence scale in the liquid phase, τ_L^t, depends thus on ζ_r. Two asymptotic cases can be considered:

(1) If the relative velocity of the dispersed phase is negligible, then ζ_r vanishes in Eq. 14. The characteristic timescale of the turbulence seen by the gas phase is equal to the characteristic time of the turbulence scale in the liquid phase; in other words, without relative velocity, the dispersed phase follows the continuous phase and behaves as a fluid particle.

(2) If the relative velocity of the dispersed phase is large, then ζ_r is large too and Eq. 14 can be written as

$$\tau_{GL}^t = \frac{\tau_L^t}{\sigma_{kL}\sqrt{C_\beta}\zeta_r}$$

Considering the previous definitions, one can show that

$$\tau_{GL}^t = \left(\frac{2}{3}\right)^{3/2} C_\mu \frac{\Lambda_L}{|\overline{V_r}|}$$

Thus, the characteristic timescale of the turbulence seen by the gas phase is related to the ratio of the Taylor macrolength scale in the liquid, Λ_L, divided by the relative velocity of the bubble. It is thus related to the time during which a bubble travels a large vortex.

In Eq. 12, the covariance $\overline{u_G' u_L'}$ is related to the turbulent kinetic energy in the liquid k_L as

$$\overline{u_G' u_L'} = 2k_L \frac{b + \eta_r}{1 + \eta_r} \tag{16}$$

where η_r is the ratio of the characteristic timescale of the turbulence seen by the gas phase, denoted τ_{GL}^t, given by Eq. 14 and the characteristic timescale of the bubble entrainment by the liquid motion, τ_{GL}^F.

$$\eta_r = \frac{\tau_{GL}^t}{\tau_{GL}^F} \tag{17}$$

τ_{GL}^F is expressed by

$$\tau_{GL}^F = \frac{2r_b}{3C_D U_r} \left(\frac{\rho_G}{\rho_L} + C_A\right) \tag{18}$$

where the parameter b is expressed as

$$b = \frac{1 + C_A}{\rho_G/\rho_L + C_A} \tag{19}$$

If the characteristic timescale of the turbulence seen by the gas phase, τ_{GL}^t, is large compared to the characteristic timescale of the bubble entrainment by the liquid motion, τ_{GL}^F, the bubble will follow the turbulent motion of the liquid phase. Thus η_r is large and $\overline{u_G' u_L'} = 2k_L$.

The added mass coefficient is taken as 0.5 and the parameter C_β is equal to 0.45.

Turbulence modeling of the continuous phase

The turbulence modeling in the continuous phase is based on the two equations (k, ε) turbulence model derived in two phase flow, including interfacial transfer of turbulent kinetic energy (TKE) and its dissipation rate. The turbulence modeling reported below was developed by Simonin and coworkers.[17,18,20]

The Reynolds stress tensor is expressed in terms of turbulent viscosity in the liquid as

$$-\overline{u_{iL}' u_{jL}'} = \nu_{tL}\left(\frac{\partial \overline{U_{jL}}}{\partial x_i} + \frac{\partial \overline{U_{iL}}}{\partial x_j}\right) - \frac{2}{3} k_L \delta_{ij} \tag{20}$$

where the turbulent viscosity is given by

$$\nu_{tL} = C_\mu \frac{k_L^2}{\varepsilon_L} \tag{21}$$

The turbulent kinetic energy (k_L, TKE) transport equation in the liquid phase is expressed as

$$\frac{\partial \rho_L \alpha_L k_L}{\partial t} + \nabla \cdot (\rho_L \alpha_L k_L \overline{U_L}) = \nabla\left(\rho_L \alpha_L \frac{\nu_{tL}}{\sigma_{kL}} \nabla k_L\right) + \alpha_L \rho_L \mathrm{Pr}_L - \alpha_L \rho_L \varepsilon_L + \Pi_{kL}^i \tag{22}$$

The transport equation of the dissipation rate of the TKE (ε_L) in the liquid phase is expressed as

$$\frac{\partial \rho_L \alpha_L \varepsilon_L}{\partial t} - \nabla \cdot (\rho_L \alpha_L \varepsilon_L \overline{U_L}) = \nabla\left(\rho_L \alpha_L \frac{\nu_{tL}}{\sigma_{\varepsilon L}} \nabla \varepsilon_L\right) + C_{\varepsilon_1} \frac{\varepsilon_L}{k_L} \alpha_L \rho_L \mathrm{Pr}_L - C_{\varepsilon_2} \alpha_L \rho_L \frac{\varepsilon_L^2}{k_L} + \Pi_{\varepsilon L}^i \tag{23}$$

Pr_L represents the classical single phase production term of turbulent kinetic energy in the liquid phase. The TKE in the liquid phase is affected by the interfacial effects; the interfacial term was modeled by Bel F'dhila and Simonin:[18]

$$\Pi_{kL}^i = \frac{\rho_G}{(\rho_G + \rho_L C_A)} \alpha_G \frac{3}{8} \rho_L \frac{C_D |\overline{V_r}|}{r_b} \left(\overline{u_G' u_L'} - 2k_L + \overrightarrow{\overline{v_d}} \cdot \overrightarrow{\overline{V_r}}\right) \tag{24}$$

Accounting for the previous discussion, assuming that $\overline{u_G' u_L'} = 2k_L$, only the term $\overrightarrow{\overline{v_d}} \cdot \overrightarrow{\overline{V_r}}$ remains in Eq. 24. It is the scalar product of the velocities that can be written as

$$\overrightarrow{\overline{v_d}} \cdot \overrightarrow{\overline{V_r}} = \overline{v_d}\,\overline{V_r} \cos(\theta)$$

where θ is the angle between the two vectors. Thus Eq. 23 becomes

$$\Pi^i_{kL} = \frac{\rho_G}{(\rho_G + \rho_L C_A)} \alpha_G \frac{3}{8} \rho_L \frac{C_D |\overrightarrow{V_r}|^2}{r_b} \overrightarrow{v_d} \cos(\theta) \qquad (25)$$

The drift velocity given by Eq. 11 can be expressed as

$$\overrightarrow{\overline{v_d}} = -D^t_{GL} \frac{1}{\alpha_G (1 - \alpha_G)} \overrightarrow{\nabla} \alpha_G$$

In addition, assuming an equilibrium between drag and buoyancy:

$$\Delta\rho \, \vec{g} = \frac{3}{8} \rho_L \frac{C_D \overrightarrow{V_r}}{r_b} \overrightarrow{\overrightarrow{V_r}} \qquad (26)$$

Thus the interfacial transfer of TKE is given by

$$\Pi^i_{kL} = -\frac{\rho_G}{(\rho_G + \rho_L C_A)} \Delta\rho D^t_{GL} \frac{1}{1 - \alpha_G} \vec{g} \cdot \overrightarrow{\nabla} \alpha_G \qquad (27)$$

Given the density of the mixture, $\rho_m = \rho_G \alpha_G + \rho_L \alpha_L$, it becomes

$$\overrightarrow{\nabla} \rho_m = -\Delta\rho \overrightarrow{\nabla} \alpha_G$$

Thus, finally

$$\Pi^i_{kL} = \frac{\rho_G}{(\rho_G + \rho_L C_A)} \frac{1}{1 - \alpha_G} D^t_{GL} \vec{g} \cdot \overrightarrow{\nabla} \rho_m = \frac{\rho_G}{(\rho_G + \rho_L C_A)} \frac{1}{1 - \alpha_G} \nabla \rho_m \, g \, D^t_{GL} \cos(\theta) \qquad (28)$$

As Haynes[21] mentioned in his PhD thesis, this term corresponds to turbulence damping by density gradient, related to gas fraction gradient. One must highlight that this term is different from zero only when the drift velocity vector and the relative velocity vector are not perpendicular. In bubble columns, bubble plumes, or airlifts, the relative velocity of the bubbles is mainly vertical (following $\vec{g}$) and the drift velocity is mainly horizontal (following $\overrightarrow{\nabla}\rho$, as previously outlined). In these cases, the interfacial transfer of TKE probably vanishes.

The dissipation rate of the turbulent kinetic energy in the liquid phase is also affected by the interfacial effects. The interfacial term was modeled by Elgobashi and Abou-Arab:[22]

$$\Pi^i_{\varepsilon L} = C_{\varepsilon_3} \frac{\varepsilon_L}{k_L} \Pi^i_{kL} \qquad (29)$$

As previously discussed, this classical term will vanish in the case of airlift reactor. This set of equations will be solved in part 4 and discussed in part 5.

Concentration transport equation

To perform tracer experiment from a numerical perspective, it is first necessary to recall the equations governing the concentration transport phenomena in the liquid phase. Because of the turbulence, local instantaneous concentration and velocity are decomposed in terms of statistical average (overbar) and turbulent fluctuation (prime) as

$$c_L = \overline{C_L} + c'_L \qquad \text{and} \qquad u_L = \overline{U_L} + u'_L \qquad (30)$$

Thus, the general transport equation of the concentration in the liquid phase is given by

$$\frac{\partial \alpha_L \overline{C_L}}{\partial t} + \nabla \cdot \alpha_L \overline{C_L U_k L} = -\nabla \cdot \alpha_k \left(\overline{J_L} + \overline{c'_L u'_L} \right) \qquad (31)$$

where $\overline{J_L}$ represents the molecular diffusion, modeled by Fick's law:

$$\overline{J_L} = -D_L \nabla \cdot C_L \qquad (32)$$

The turbulent diffusion of the concentration in the liquid is expressed in terms of turbulent diffusivity D_{tL}:

$$-\overline{c'_L u'_L} = D_{tL} \nabla \overline{C_L} \qquad (33)$$

where the turbulent diffusivity D_{tL} is proportional to the turbulent viscosity and has the same order of magnitude:

$$D_{tL} = \frac{\nu_{tL}}{\mathrm{Sc}_t} \qquad (34)$$

given that the turbulent Schmidt number (Sc_t) is close to 1. It expresses that the same turbulent structures diffuse both the momentum and the concentration attached to fluid particles.

The equation of transport of concentration in the liquid is thus

$$\frac{\partial \alpha_L \overline{C_L}}{\partial t} + \nabla \cdot \alpha_L \overline{C_L} \; \overline{U_L} = \nabla \cdot \alpha_L ((D_L + D_{tL}) \nabla \overline{C_L}) \qquad (35)$$

It will be solved and discussed later.

Experimental

Most of the experimental data related to the gas–liquid airlift reactor, referred to herein, were carried out by Couvert.[13] Detailed information is given in Couvert et al.[23,24]

The reactor is a parallelepiped vessel, 3 m high and 0.5 m wide and deep, equipped with a baffle in its middle as described in Figure 1. The baffle position is fixed. The reactor was initially filled with tap water, up to 2.6 m high. The pilot is divided into four sections: an upward flow aerated section; the free surface flow above the internal wall; a downward flow less aerated section, usually called downcomer; and the flow below the internal wall, including the gas injector, usually called sparger. The liquid height below the internal wall is 150 mm.

The global circulation of liquid is induced by air injection, which is ensured by two horizontal cylindrical membrane spargers (Flexazur® T415 membrane covering Plexiglas® cylinders), located at the bottom right of the reactor. The outside diameter of each cylindrical membrane sparger is 40 mm. The axis of the cylindrical membrane spargers is located at 100 mm above the bottom of the pilot. Because the injectors were made from a perforated membrane, the bubble diame-

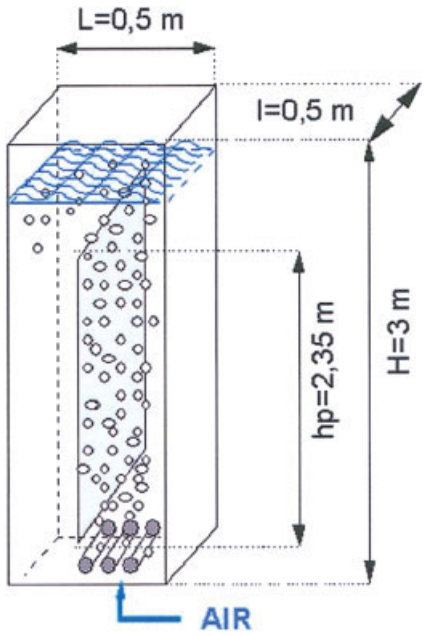

Figure 1. Experimental airlift reactor pilot.

[Color figure can be viewed in the online issue, which is available at www.interscience.wiley.com.]

ters are calibrated by the superficial gas velocity as shown by Couvert,[13] who measured the bubble diameters for different superficial gas velocities. Bubble size was visualized by video camera (Sony DXC 930 P, 3 CCD[23]).

Measurement of gas fraction

Holes distributed along the height of the reactor walls ensure the pressure measurement, from which volume gas fraction is deduced. This technique is well adapted when flow is fully developed and when the pressure gradient is mainly controlled by the gravity term. Longitudinal distributions of gas fraction in both upward and downward flow sections have thus been estimated. The overall gas holdup in the airlift is determined by using a volume expansion technique and is measured from the difference between the ungassed and gassed liquid level (Table 1).[13]

Measurement of liquid velocity

The liquid velocity field in the nonaerated zone at the bottom of the downflow was previously measured with PIV (particle image velocimetry) system by Cockx.[14] Details on the PIV system acquired from Dantec Measurement Technology were given in Bugay et al.[25] The system used was a 4-W continuous wave laser (Innova 70-4 from Coherent, argon-ion source), an electrooptical shutter, an optical fiber, a polygon scanner, and a double image 700 recorder camera (CCD camera, 768 × 484 pixels[2]).

Table 1. Experimental Data after Couvert (2000)

Gas flow rate (L/s)	0.62	2.12	5.62
Superficial gas velocity (cm/s)	0.5	1.7	4.5
Mean gas fraction	0.8	2.6	7.0
Mean gas fraction in the riser	1.1	3.4	7.6
Mean gas fraction in the downcomer	0.6	1.8	6.5
Bubble Sauter diameter (mm)	2.7	3.4	4.3

Measurement of concentration

During the salt tracing technique, concentration is tracked by a conductimeter probe (Model XE 100, Tacussel, Inc. Villeurbanne, France) connected to a conductimeter (Tacussel type CD 6N) and a computer. This device also allows the measurement of mixing parameters from which the liquid velocity and axial dispersion are deduced. This technique was applied by Couvert et al.[23] It consists in injecting a quantity of NaCl. From the measurement of concentration vs. time, one can see that after four loops, the concentration is completely mixed in the reactor. In addition, each loop (of length $L = 5$ m) corresponds to a circulation time t_c equal to 25 s and to a velocity U_L of 0.2 m/s. The global expression of the transport equation of salt is recalled:

$$\frac{\partial C_L}{\partial t} + U_L \frac{\partial C_L}{\partial z} = E_{ZL} \frac{\partial^2 C_L}{\partial z^2} \tag{36}$$

The curve giving the concentration vs. time can be fitted by the Voncken model expressed in terms of nondimensional temporal variable $\theta = t/t_c$ and nondimensional concentration variable $E = C/C_0$, where C_0 is the completely mixed value of concentration:

$$E = \frac{1}{2}\sqrt{\frac{\mathrm{Pe}}{\pi\theta}} \sum_{j=0}^{\infty} \exp\left[-\frac{\mathrm{Pe}(j-\theta)^2}{4\theta}\right] \tag{37}$$

After fitting the experimental curve $C_L(t)$, corresponding to a superficial gas velocity of 1.7 cm/s, the Peclet number ($\mathrm{Pe} = U_L L/E_{ZL}$) was 30, which corresponds to an axial dispersion coefficient of 0.04 m^2/s.

In addition, from the experimental curve $C_L(t)$, the mixing time can be determined : it is defined as the number of loops (circulation time of the liquid in the airlift), needed to have a uniform distribution of the concentration within the airlift. Experimental data of the nondimensional concentration $E = C/C_0$, are reported in Table 2, as a function of the nondimensional time, $\theta = t/t_c$. After four loops, the gap between the local concentration and the theoretical value, corresponding to a perfectly mixed reactor C_0, is of the order of magnitude of 1%.

CFD tool

Commercial Fluent® code version 6 was used to solve continuity and momentum equations. The pressure–velocity coupling is obtained using a "Phase Couple SIMPLE" algorithm. For the convective terms of the conservation equations, a first-order UPWIND differencing scheme is applied. As soon as convergence is reached, a QUICK differencing scheme is implemented, offering a more accurate result than the UPWIND scheme as recommended by Sokolichin et al.[26] All the simulations were carried out using two-dimensional (2D, 13,200 cells) and three-dimensional (3D, 62,900 cells) meshes. The geometry and the meshes are performed with the preprocessor GAMBIT. Detailed information is reported in Talvy.[27]

Table 2. Evolution of $E = C/C_0$ According to Mixing Time

θ experimental	1	2	3	4
E experimental	1.52	1.12	1.04	1.01

Validation of Numerical Simulation of Hydrodynamics

Before presenting the numerical simulations, it is necessary to recall the global behavior of the airlift reactor. Indeed, the liquid circulation induced by the gas flow results from a balance between (1) the difference of column weight between upward and downward flow sections, and (2) the total pressure drops, in which the singular ones are much more important than the linear ones in our experiment.

The global momentum balance can be expressed as follows:[5,16,28]

$$[(\rho_g R_{gd} + \rho_l R_{ld})g - (\rho_g R_{gu} + \rho_l R_{lu})g]H = \left[\frac{P_{wu}\tau_{wu}}{S_u} + \frac{P_{wd}\tau_{wd}}{S_d}\right]H + \Delta P_2 + \Delta P_3 \quad (38)$$

The left-hand side of the equation represents the difference of weight between the upward flow section (index u) and the downward one (index d). ρ is the density and R is the cross-sectional average of local phase fraction α, in the gas (index g) or in the liquid (index l). H is the height of the internal wall. The right-hand side of the equation comprises the linear pressure drop, where P denotes wall (index w) perimeters wetted by the liquid, τ represents the wall shear stress, and S the cross sections of upward and downward flows. ΔP_2 and ΔP_3 account for singular pressure drops, respectively, above and below the internal wall. The right-hand side terms will thus be proportional to the square of the liquid velocity. In the airlift, the gas flow rate is imposed, but the liquid velocity induced by the aeration is unknown. Because this liquid velocity results from the previous balance, its determination will depend on both the estimation of gas fraction distribution in the airlift (left-hand side of Eq. 38) and on the correct representation of the singularities, in terms of pressure drops (right-hand side of Eq. 38).

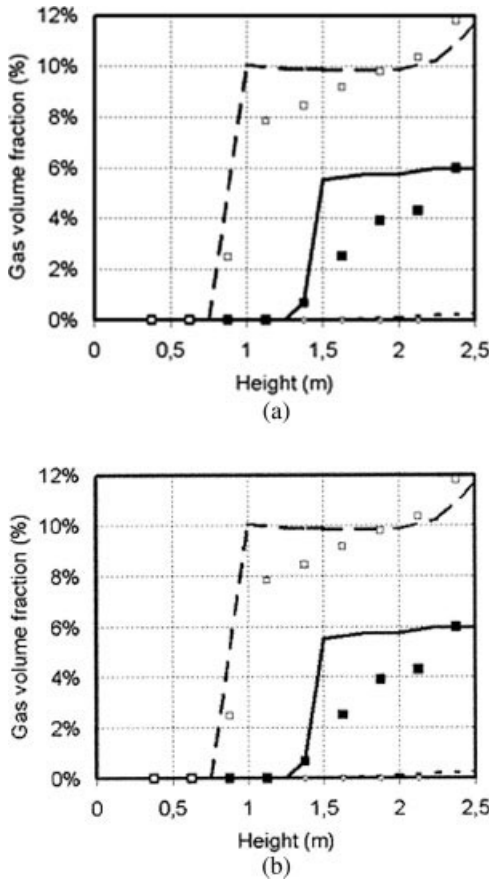

Figure 2. Gas volume fraction distribution in riser (a) and downcomer (b) for three gas superficial velocities.

$j_g = 0.5$ cm/s (◇: Experiment; - - -: CFD); $j_g = 1.7$ cm/s (■: Experiment; —: CFD); $j_g = 4.5$ cm/s (□: Experiment; – – –: CFD).

Modeling in the airlift

In the simulations, the reference case is based on the following modeling assumptions: free surface deformation, drift velocity, drag coefficient,[19] source terms in the k–ε model, and without added mass. In addition, simulations are first made in 2D.

Longitudinal distribution of gas in the airlift

Figures 2a and 2b represent the longitudinal distribution of the gas volume fraction for three different superficial gas velocities (0.5, 1.7, 4.5 cm/s). In the riser part (Figure 2a), it can be seen that the CFD results are in good agreement with the experiments. One meter above the injector, the flow can be considered as fully developed because, downstream, the gas volume is nearly constant (roughly 1% for 0.5 cm/s, 4% for 1.7 cm/s, and 8.5% for 4.5 cm/s). Looking at the gas volume fraction distribution in the downcomer (Figure 2b), for a superficial gas velocity equal to 0.5 cm/s, the downcomer is not aerated, as shown by experimental results and confirmed by CFD results. For the two other superficial gas velocities, the main remark is that the length of the aerated region at the top of the downcomer is well predicted. This height is equal to about 1.4 m for 1.7 cm/s and 0.75 m for 4.5 cm/s. However, predicted gas distribution is slightly different from the experimental results. For gas velocity equal to 1.7 cm/s, the predicted gas fraction between 1.5 and 2.25 m is higher than experimental values. In recirculating flow regions, at the bottom of the riser and at the top of the downcomer, the flow is accelerated and decelerated; thus, the measurement of pressure gradient does not enable us to assess the local gas fraction. In addition, the zone at the top of the downcomer is actually a recirculation, where coalescence may occur. It is not taken into account in the modeling. To complete the study in terms of gas distribution, the radial gas distribution is studied.

Horizontal profile of gas fraction in the airlift

Couvert[13] measured bubbles radial distributions in the riser. The superficial gas velocity is equal to 1.7 cm/s. At the position in the riser (2.125 m), as the flow is well developed and steady, CFD results are in good agreement with experimental data (Figure 3).

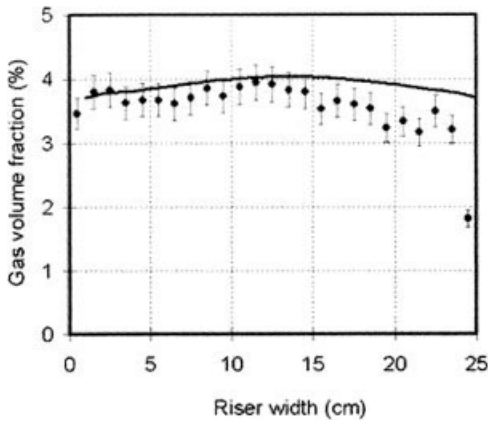

Figure 3. Horizontal profile of gas fraction in riser.

●: Experiment; —: CFD.

Longitudinal profile of liquid velocity in the airlift

Cockx[14] measured a velocity profile in the nonaerated zone of the downcomer at one height. The superficial gas velocity is equal to 1.7 cm/s. The predicted velocity profile is plotted on Figure 4 and compared to PIV experiments. The agreement is very good. The order of magnitude of the liquid velocity is equal to 0.20 m/s.

Discussion on Numerical Simulation of Hydrodynamics

Once validated, the model has to be analyzed. The sensitivity analysis is limited to the superficial velocity of 1.7 cm/s. The goal of the discussion is to determine the most important parameters in the modeling of two-phase bubbly flow, in the case of an airlift reactor. The most important one is the drift velocity, necessary to correctly account for the bubble dispersion by the turbulence of the liquid. As will be shown later, this term cannot be ignored. The second important issue concerns the drag coefficient. Different models are tested. The third sensitivity analysis is based on the treatment of the free surface; considering it as a fixed surface simplifies the simulation but biased the result. Finally, the necessity to simulate in 3D or the possibility to limit the simulation in 2D is discussed.

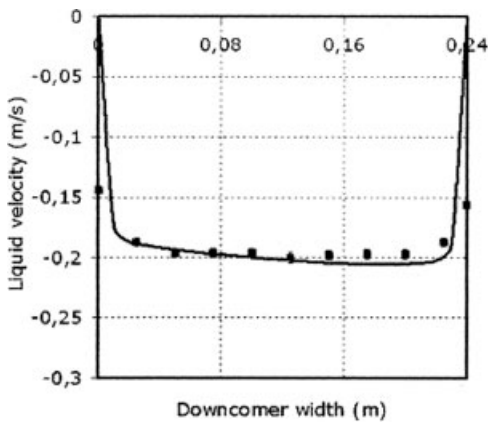

Figure 4. Horizontal profile of liquid velocity in downcomer.

■: Experimental; —: CFD.

Drift velocity and added mass

The effects of the drift velocity and added mass were investigated first. Different simulations were made with and without drift velocity, with and without added mass. The sensitivity of the model to these closure relations can be discussed from Figure 5. The longitudinal distributions of gas fraction in the riser are plotted. Predicted values under different modeling hypothesis (without added mass with drift velocity, without added mass without drift velocity, with added mass with drift velocity) are compared to experimental data. The main conclusion of the sensitivity analysis to drift velocity and added mass is the significant effect of drift velocity, to correctly predict gas fraction dispersion. Indeed, the drift velocity enables to reproduce the dispersion of the gas bubbles in the turbulent liquid flow. Without accounting for the drift velocity, the gas plume is not dispersed over the cross-section in the riser (Figure 5), overestimating the gas velocity and underestimating the gas fraction. To better understand this phenomenon, it is interesting to come back to the modeling of the drift velocity:

$$\overline{v_d} = -D^t_{GL}\left[\frac{1}{\alpha_G}\nabla\alpha_G - \frac{1}{\alpha_L}\nabla\alpha_L\right] \tag{39}$$

where the fluid-bubble turbulent dispersion term is modeled as (Eq. 12)

$$D^t_{GL} = \frac{1}{3}\tau^t_{GL}\overline{u'_G u'_L}$$

τ^t_{GL} is the characteristic timescale of the turbulence seen by the gas phase; it is related to the characteristic time of the turbulence scale in the liquid phase. It can be written as

$$\tau^t_{GL} = \frac{1}{\sigma_{kL}}\frac{3}{2}C_\mu\frac{k_L}{\varepsilon_L}\left(1 + C_\beta\zeta_r^2\right)^{-1/2} \tag{40}$$

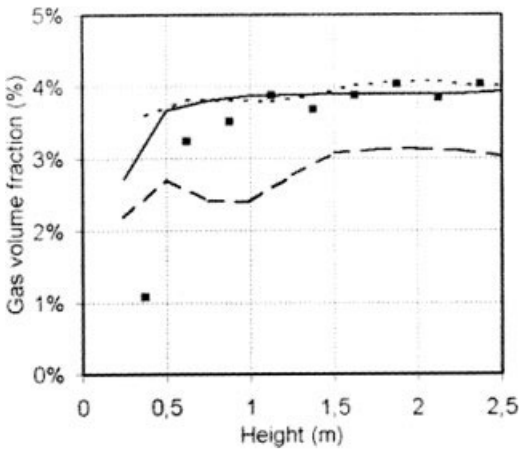

Figure 5. Sensitivity of gas volume fraction in riser to added mass and drift velocity.

■: Experiment; —: without added mass, with drift velocity, predictions; – – –: without added mass, without drift velocity; - - -: with added mass, with drift velocity.

In addition, the covariance $\overline{u'_G u'_L}$ is related to the turbulent kinetic energy in the liquid k_L:

$$\overline{u'_G u'_L} = 2k_L \frac{b+\eta_r}{1+\eta_r} \tag{41}$$

Thus, the fluid-bubble turbulent dispersion term becomes

$$D^t_{GL} = \frac{1}{\sigma_{kL}} C_\mu \frac{k_L^2}{\varepsilon_L} \left(1 + C_\beta \zeta_r^2\right)^{-1/2} \frac{b+\eta_r}{1+\eta_r} \tag{42}$$

It is thus clear that the fluid-bubble turbulent dispersion is proportional to the turbulent viscosity in the liquid [$v_{tL} = C_\mu(k_L^2/\varepsilon_L)$]. It is affected by two corrective terms. The first one depends on ζ_r, the ratio of the characteristic time of the turbulence in the liquid, and the characteristic timescale of the bubble necessary to cross the containing energy eddies:

$$\zeta_r = \frac{|\overline{U_r}|}{\sqrt{2k_L/3}} \tag{43}$$

In fact, the turbulent kinetic energy varies between its value in the wall region $k_L = U^{*2}/\sqrt{C_\mu}$ and around 1/3 of this value far from the wall. In addition, the friction velocity U^* is roughly equal to 5% of the mean velocity. Thus, ζ_r can be estimated as

$$\zeta_r = \frac{|\overline{U_r}|}{\sqrt{2/3\sqrt{C_\mu}}5\%U_L} = 13\frac{|\overline{U_r}|}{U_L} \tag{44}$$

It was found from the simulation that the liquid velocity is of the same order than the slip velocity of the bubbles. Thus, ζ_r equals 13. Because C_β is of the order of 0.45, the corrective term can be simplified:

$$\left(1 + C_\beta \zeta_r^2\right)^{-1/2} \approx \frac{1}{\sqrt{C_\beta}\zeta_r} \approx 0.1 \tag{45}$$

The second corrective term in Eq. 42 is related to $(b + \eta_r)/(1 + \eta_r)$, where η_r is the ratio of the characteristic timescale of the turbulence seen by the gas phase, denoted τ^t_{GL} and the characteristic timescale of the bubble entrainment by the liquid motion τ^F_{GL}:

$$\eta_r = \frac{\tau^t_{GL}}{\tau^F_{GL}} = \frac{\frac{1}{\sigma_{kL}}\frac{3}{2}C_\mu \frac{k_L}{\varepsilon_L}\left(1 + C_\beta\zeta_r^2\right)^{-1/2}}{\frac{2r_b}{3C_D U_r}\left(\frac{\rho_G}{\rho_L} + C_A\right)} = \frac{C_\mu C_D}{\sigma_{kL}\sqrt{C_\beta}} \times \frac{9}{4}\sqrt{\frac{2}{3}}\frac{{k_L}^{3/2}}{\varepsilon_L r_b}\frac{1}{\left(\frac{\rho_G}{\rho_L} + C_A\right)} = 0.25\frac{\Lambda_L}{r_b}\frac{1}{\left(\frac{\rho_G}{\rho_L} + C_A\right)} \tag{46}$$

where Λ_L is the Taylor macroscale of the turbulence in the liquid phase. It is mainly related to the geometry of the airlift, in particular to the distance to the wall.

The corrective factor becomes

$$\frac{b+\eta_r}{1+\eta_r} = \frac{\frac{1+C_A}{\left(\frac{\rho_G}{\rho_L} + C_A\right)} + 0.25\frac{\Lambda_L}{r_b}\frac{1}{\left(\frac{\rho_G}{\rho_L} + C_A\right)}}{1 + 0.25\frac{\Lambda_L}{r_b}\frac{1}{\left(\frac{\rho_G}{\rho_L} + C_A\right)}} = \frac{1 + C_A + 0.25\frac{\Lambda_L}{r_b}}{\frac{\rho_G}{\rho_L} + C_A + 0.25\frac{\Lambda_L}{r_b}} \approx \frac{1 + C_A + 0.25\frac{\Lambda_L}{r_b}}{C_A + 0.25\frac{\Lambda_L}{r_b}} \tag{47}$$

Because the bubbles are small compared to the size of the airlift, $\Lambda_L/r_b \gg 1$, thus the corrective factor is equal to unity, whatever the added mass coefficient value C_A. We can thus understand why the gas dispersion weakly is sensitive to added mass (Figure 6). Finally, the fluid-bubble turbulent dispersion term becomes

$$D^t_{GL} = \frac{0.1}{\sigma_{kL}} C_\mu \frac{{k_L}^2}{\varepsilon_L} \tag{48}$$

Recall the definition of the drift velocity:

$$\overrightarrow{\overline{v_d}} = -D^t_{GL}\frac{1}{\alpha_G(1-\alpha_G)}\vec{\nabla}\alpha_G$$

In fully developed upward flow, the vertical gradient of gas fraction $\partial\alpha_G/\partial z$ is null and thus the vertical component of the drift velocity is also null: $\overline{v_{dz}} = 0$. The vertical component of the drift velocity $\overline{v_d}$ is negligible compared to the longitudinal (vertical) relative velocity $\overline{U_r}$. However, horizontal gradient of gas fraction induces horizontal drift velocity:

$$\overline{v_{dx}} = -D^t_{GL}\frac{1}{\alpha_G(1-\alpha_G)}\frac{\partial\alpha_G}{\partial x}$$

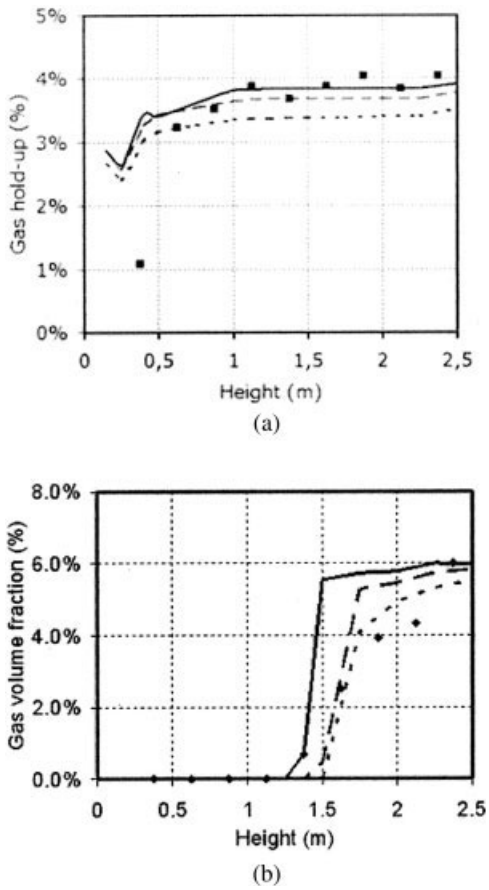

Figure 6. Sensitivity of gas volume fraction to the drag law coefficient in riser (a) and downcomer (b).

■: Experiment; —: Karamavev; – – –: Clift et al.; - - -: Harmathy.

If the gas fraction is high in the bulk of a gas plume and null outside the gas plume, the gas fraction horizontal gradient $\partial\alpha_G/\partial x$ is negative and thus it induces a positive drift velocity, generating gas dispersion.

According to many authors,[12,17,26] the added mass effect is crucial in a partially aerated bubble column to account for the oscillation of the bubble plumes, for example. Becerril also noticed that the value of the added mass coefficient must not be constant and must be dependent on the local gas fraction and the shape of the bubbles. In Fluent® code, the added mass coefficient is fixed to 0.5. According to Figure 5, the added mass coefficient has no significant effect in the riser, where the flow is well developed with an average gas volume fraction of roughly 4%. In the first meter above the injection of gas, where the flow is accelerated, added mass tends to increase the gas dispersion. Mudde and van den Akker[6] simulated airlift reactor with added mass force, but did not mention any discrepancies concerning this effect. In an airlift reactor (Figure 5 and Eq. 47), added mass is shown to play a minor role.

A last comment on interfacial transfer is related to the transfer of turbulence. Because η_r is given by Eq. 46 and because $\Lambda_L/r_b \gg 1$, the corrective factor given by Eq. 47 is equal to unity. Thus, the covariance $\overline{u'_G u'_L}$ is equal to twice the turbulent kinetic energy in the liquid k_L. Consequently, the interfacial transfer of turbulent kinetic energy given by Eq. 24 does vanish.

In conclusion, the zones of gas fraction gradient contribute to gas dispersion (in the momentum equation) but do not contribute to enhancement or damping of turbulence (in the TKE equation). In addition, drift velocity modeling affects the horizontal velocity of bubbles, in terms of gas dispersion, but does not affect the longitudinal (vertical) transfer of momentum between the gas and the liquid. Thus, the liquid velocity, in terms of liquid circulation, is not affected by the drift velocity modeling.

Drag coefficient

As shown earlier, the hydrodynamics in the airlift is based on a balance between aeration difference (between the riser and the downcomer) and pressure drops. Aeration is quantified in terms of gas fraction, itself resulting from interfacial momentum transfer between gas bubbles and the liquid phase. Considering the bubble diameter as an input of the simulations, the interfacial momentum transfer is controlled by the modeling of the drag coefficient. A classical drag law, proposed in CFD code, is attributed to Schiller and Naumann:[10]

$$C_D = \frac{24}{\mathrm{Re}}(1 + 0.15\mathrm{Re}^{0.687}) \qquad \text{for} \qquad \mathrm{Re} < 1000 \tag{49a}$$

$$C_D = 0.44 \qquad \text{for} \qquad \mathrm{Re} > 1000 \tag{49b}$$

Indeed, this correlation was developed for solid spheres. This correlation can be modified to account for dispersed phase volume fraction. In our experiments, because the gas fraction is very small, this correction has not been accounted for. In general, bubbles are distorted. Thus, r_b in Eq. 5 is the radius of a sphere of volume equivalent to that of the distorted bubble. It is thus possible to introduce the eccentricity of the bubble in the expression of the projected area, assuming an ellipsoidal shape for the bubble with a circular horizontal projected area (diameter b) and a vertical smaller axis c. The eccentricity is $E = c/b$. Then, the projected area is given by

$$a_p = \frac{3}{2}\frac{\alpha_G}{b} = \frac{3}{4}\frac{\alpha_G}{r_{beq}E^{2/3}} \tag{50}$$

For the sake of simplicity, the effect of distortion can be included in the expression of the drag coefficient and equivalent bubble radius can be used.

$$C_{Deq} = \frac{C_D}{E^{2/3}} \qquad \text{with} \qquad \overline{I_{DG}} = \alpha_G \rho_L \frac{3C_{Deq}}{8r_{beq}}|\overline{V_r}|\overline{V_r} \tag{51}$$

For example, given an eccentricity E of 30% (corresponding to a bubble diameter of several millimeters[9]), the equivalent drag coefficient is doubled. Given that the bubble Reynolds number is of the order of 1000, the drag coefficient of a solid sphere 0.45 becomes 0.9 for an ellipsoid with an eccentricity of 30%. This value is surprisingly close to the value proposed by Karamanev and Nikolov[19] and is used in the present simulations.

Van Baten et al.[7] used another correlation proposed by Clift et al.[9] They verified that the rise velocity is well represented with a correlation, where the drag coefficient depends only on the Eötvös (Eö) number:

$$C_D = \frac{2}{3}\sqrt{\mathrm{E\ddot{o}}} \qquad \text{with} \qquad \mathrm{E\ddot{o}} = \frac{(\rho_l - \rho_g)}{\sigma} g d_b^2 \tag{52}$$

Given a bubble diameter (d_b) equal to 3.4 mm, the drag coefficient C_D is equal to 0.84. This value is again twofold larger than the value calculated from the correlation proposed by Schiller and Naumann[10] arising from the fact that, for Eö $>$ 1, bubbles are not spherical but ellipsoidal and thus have a higher drag coefficient.

Another modeling of the drag mainly used in gas–liquid flow simulations was proposed by Harmathy.[29] He proposed a constant slip velocity of the bubbles when their Reynolds number is of the order of 1000. The slip velocity is given by

$$\overline{U_r} = 1.5\left(\frac{\sigma g \Delta\rho}{\rho_L^2}\right)^{1/4} \tag{53}$$

which corresponds to a constant slip velocity of 0.25 m/s. It corresponds to a drag coefficient expression very close to the previous one because it can be written as

$$C_D = 0.56\sqrt{\mathrm{E\ddot{o}}} \tag{54}$$

In this case, the drag coefficient C_D is equal to 0.7.

The sensitivity of the simulations to these three types of coefficients was tested.[9,19,29] Figure 6 presents the longitudinal distributions of the gas volume fraction in the riser and in the downcomer. The relative velocity of the bubbles increases with decreasing drag coefficient. Thus the volume fraction of the gas decreases with decreasing drag coefficient. Consequently, in the riser, the experimental gas fraction is well predicted with the correlation of Karamanev and Nikolov[19] but is weakly underestimated with the Clift et al.[9] expression and is further underestimated with the Harmathy[29]

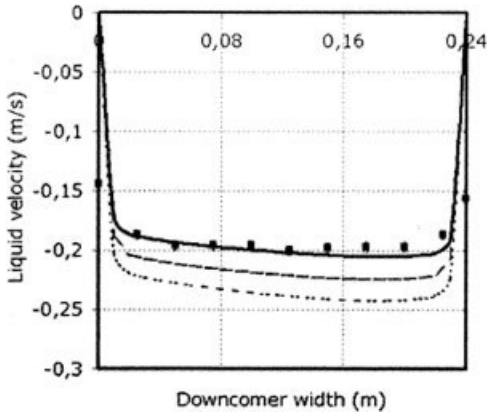

Figure 7. Sensitivity of axial liquid velocity in downcomer to drag law coefficient.

■: PIV experiment; —: Karamavev; – – –: Clift et al.; - - -: Harmathy.

correlation. In the downcomer, the velocity of the gas decreasing with decreasing drag coefficient, the height of the aerated zone is correctly predicted with the correlation of Karamanev and Nikolov[19] but is underestimated with the Clift et al.[9] expression and more underestimated with the Harmathy[29] correlation. Aeration of this zone also decreases with decreasing drag coefficient.

The sensitivity of predicted liquid velocity profile to drag coefficient modeling is also investigated. According to Figure 7, which represents the liquid axial velocity profile vs. the width of the downcomer, numerical simulation performed with the Karamanev–Nikolov relation,[19] for the drag coefficient, is in good agreement with the experimental profile. Indeed, with decreasing value of drag coefficient, the liquid velocity is overestimated.

The three drag coefficients (0.95, 0.86, and 0.7) correspond to respective relative velocity of 0.21, 0.23, and 0.25 m/s. It is surprising to note that the liquid velocity profiles plotted in Figure 7 correspond to superficial liquid velocities of 0.195, 0.215, and 0.23 m/s, respectively. Thus, it appears that the superficial liquid velocity is closely related to the relative velocity of the bubbles, itself imposed by the drag coefficient. In other words, the superficial liquid velocity seems to be fixed by the relative velocity of the bubbles. Physically, the consequence of this remark is that, as soon as the bubbles are entrained by the liquid in the downcomer, their average velocity is null because their upward relative velocity is equal to the downward liquid velocity.

Free surface

In the simulations, there are two ways to account for the free surface:

(1) It may be considered as a fixed (nondeformable) surface, on which is implemented a "degassing" boundary condition, where the gas can escape at the interface. Such a condition was unavailable in Fluent® code, but has been programmed in C language.

(2) It may be considered as a moving (deformable) surface. This moving interface accounts for the expansion of the liquid resulting from gas injection. In this case, the numerical domain includes a region above the liquid surface, filled with gas. The boundary condition at the top is a pressure outlet. A degassing boundary condition allows us to eliminate the interface simulation, whereas saving mesh resolution and time calculation by not simulating the part above the free surface is not simulated.

As shown in Figures 8a and 8b, the simulation of gas volume fraction in the riser and in the downcomer is dependent on the modeling of the upper surface of liquid. Fixed surface simulation is compared to free surface simulation. According to Figure 8a, the nature of the free surface has almost no influence on the gas volume fraction in the riser because the gas fraction distribution is very close in the two simulations. Modeling the free surface deformation is important to correctly predict the flow in the downcomer. A fixed surface will bias calculation of the global circulation of liquid inducing wrong values for gas volume fraction entrained in the downcomer. However, in the downcomer (Figure 8b) with the fixed surface condition, the bubbles are dragged deeper, and thus the gas volume fraction in the aerated part is smaller than that in the case with a free surface flow. This trend is directly related to the simulation of the liquid velocity (Figure 9). A fixed surface generates a larger pressure drop at the top of the airlift, inducing a larger liquid velocity.

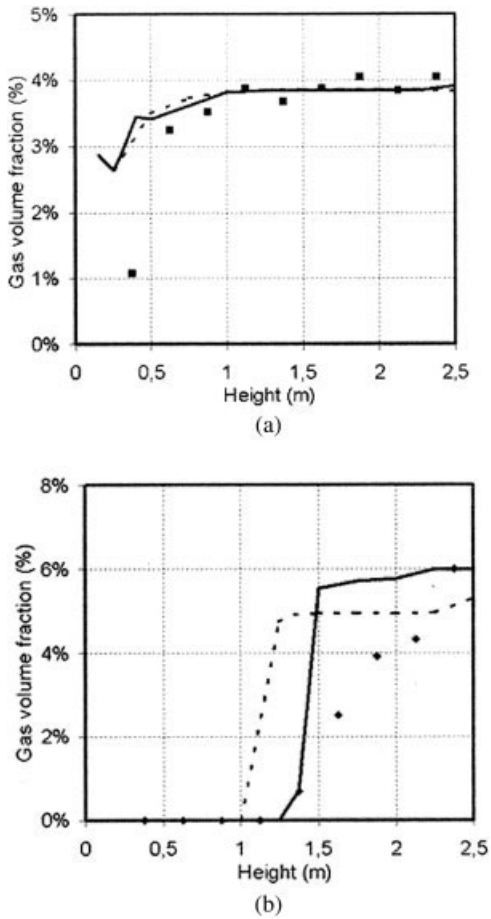

Figure 8. Sensitivity of gas volume fraction to the surface modeling in riser (a) and downcomer (b).

■: Experiment; —: Free surface; - - -: Fixed surface.

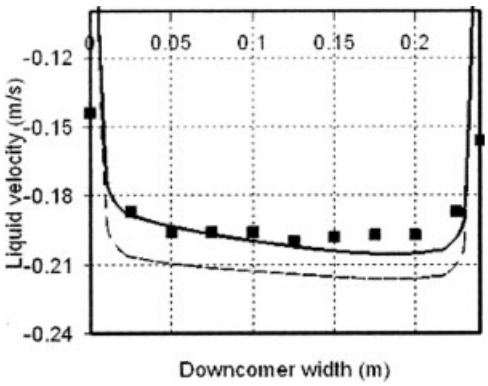

Figure 9. Sensitivity of liquid velocity in downcomer to the surface modeling.

■: PIV experiment; —: Free surface; - - -: Fixed surface.

This larger liquid velocity overestimates the entrainment of gas bubbles in the downcomer and underestimates the gas fraction.

3D vs. 2D simulations

3D simulations were run with the same modeling as that of the 2D calculations, with respect to the drag coefficient and the free surface, and where added mass force was not considered. Figures 10a and 10b present a comparison of longitudinal distribution of the gas volume fraction in the riser and in the downcomer, predicted in 2D and in 3D simulations. The results obtained in 3D simulations are in agreement with experimental data and close to the results obtained with a 2D simulation, for the superficial gas velocity of 1.7 cm/s. According to Table 3, the global gas fraction obtained from 3D simulations agrees with the experimental measurements and is slightly more accurate than the global gas fraction calculated from 2D simulation. The longitudinal profiles presented in Figures 10a and 10b confirm that the global gas volume fraction in the downcomer is better estimated with 3D simulation. In the riser, the 3D gas volume fraction remains remarkably close to the experimental values.

Once local hydrodynamics has been validated and two-fluid local modeling has been analyzed, CFD simulations based on transient transport of concentration on steady-state hydrodynamics can be discussed.

Table 3. Global Gas Volume Fraction in 2D and 3D Simulation

Global Gas Holdup	Riser	Downcomer
Experimental	3.4 ± 1%	1.8 ± 0.3%
CFD 2D	3.7%	2.5%
CFD 3D	3.3%	2.3%

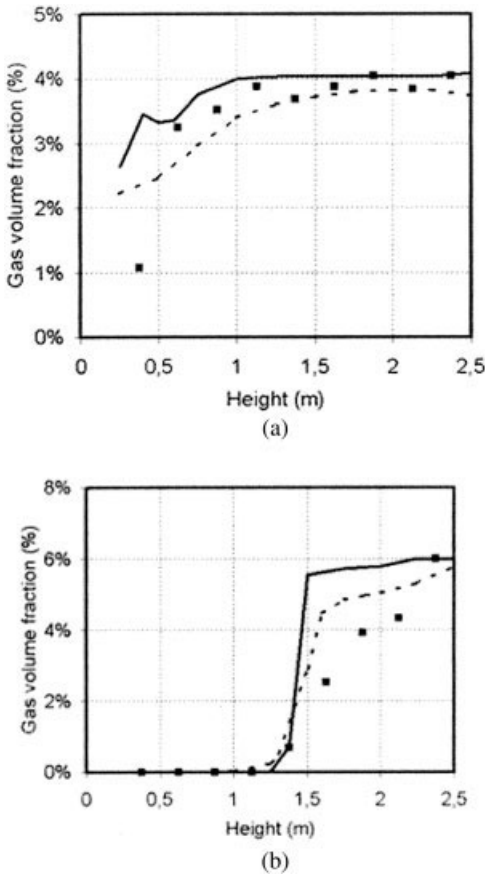

Figure 10. Gas volume fraction in riser (a) and downcomer (b) for 2D and 3D geometry.

■: Experiment; —: 2D result; - - -: 3D result.

Numerical Simulations of Axial Dispersion of a Tracer in the Liquid Phase

To characterize the global hydrodynamics within the airlift loop reactor, a numerical tracer is compared to the experimental tracer method. The efficient variables in this study are the global liquid velocity (U_L) and the Peclet number (Pe), characteristics of the axial dispersion (E_{ZL}). The objective of this section is to test the ability of CFD to simulate axial dispersion in the airlift reactor. Consequently, a numerical experiment is performed, in exactly the same way as in the laboratory pilot experiment. Concentration of salt is injected at the top of the airlift, the flow being steady state. A local probe measures the concentration of salt vs. time. In Figure 11, numerical tracer concentration vs. time is plotted

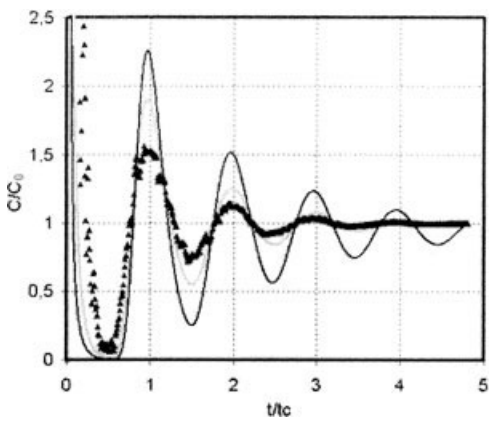

Figure 11. Numerical tracer in 2D and 3D geometry.

▲: Experiment; —: 2D; —: 3D.

Table 4. Experimental and Numerical Values of t_c, Pe, and E_{ZL}

	t_c (s)	Pe	E_{ZL} (m^2/s)
Experiment	25	30	4×10^{-2}
2D	25	80	1.5×10^{-2}
3D	23	42	2.9×10^{-2}

for both 2D and 3D simulations and compared to experiments. Time is normalized by the circulation time (t_c), that is, the time necessary to perform one circulation loop in the airlift reactor. The experimental data and the simulated concentrations predicted in 2D and 3D are interpreted thanks to the Voncken model, which provides the Peclet number and time circulation related to a timescale.

Circulation time

From Figure 11, Table 4 was prepared. According to Table 4, both 2D and 3D simulations give an accurate value of the circulation time compared to the experimental measurement (that is, about 25 s) because circulation time is directly related to liquid velocity (previously validated).

Mixing time

From Table 5, it can be noticed that experimental value of the concentration is uniformly distributed after four loops of circulation, which is not the case in the 2D simulation. 3D simulation is yet able to reproduce this phenomenon. Table 5 presents the values of maxima of $E = C(t)/C_0$ at each $\theta = t/t_c$. After four loops, the gap between local instantaneous concentration and the uniform concentration is 10% for 2D simulation and 2% for 3D simulation. To explain this gap between 2D and 3D simulations, axial dispersion is investigated.

Axial dispersion and Peclet number

In terms of Peclet number or axial dispersion, the 2D simulation is not relevant (Table 4). Indeed, the effect of the spatial dispersion is clearly dampened, explained by the fact that only two dimensions are considered, whereas the 3D Peclet number is closer to the experimental results as the result of a better estimation of the spatial dispersion. The 3D simulation is thus able to predict the mixing in the airlift reactor. However, the 3D Peclet number is slightly higher than experimental value. This result is discussed below.

Discussion on Numerical Simulations of Axial Dispersion of a Tracer in the Liquid Phase

With respect to the numerical tracer method, the aim of this section is first to determine the different contributions to axial dispersion, in terms of molecular, numerical, turbulent, and spatial diffusion or dispersion. Thus, each component is estimated and the main contribution of spatial dispersion to axial dispersion is shown. Finally, 3D simulation enables us to improve the prediction of axial dispersion. CFD results are then analyzed to improve the physical understanding of axial dispersion.

Theoretical background

In a first step, Eq. 36 will be established, to determine the different contributions to axial dispersion. Define the spatial average of volume fraction of the phase k, α_k, as R_k with $\langle\ \rangle$ the spatial averaging operator:

$$R_k = \langle \alpha_k \rangle = \frac{1}{S} \iint_A \alpha_k dS \tag{55}$$

Given a function F_k

$$R_k \langle\langle F_k \rangle\rangle = \langle \alpha_k F_k \rangle = \frac{1}{S} \iint_A \alpha_k F_k dS \tag{56}$$

and

$$R_k \langle\langle U_k F_k \rangle\rangle = \langle \alpha_k U_k F_k \rangle = \frac{1}{S} \iint_A \alpha_k U_k F_k dS \tag{57}$$

Indeed $\langle\langle U_k F_k \rangle\rangle \neq \langle\langle U_k \rangle\rangle \langle\langle F_k \rangle\rangle$ because the variables U and F are not uniformly distributed in the section. The difference between these terms represents the spatial dispersion:

$$U_k = \langle\langle U_k \rangle\rangle + \tilde{U}_k$$

$$F_k = \langle\langle F_k \rangle\rangle + \tilde{F}_k$$

then

$$\langle\langle U_k F_k \rangle\rangle = \langle\langle U_k \rangle\rangle \langle\langle F_k \rangle\rangle + \langle\langle \tilde{U}_k \tilde{F}_k \rangle\rangle \tag{58}$$

The spatial averaging of the transport equation of the concentration (Eq. 35) is expressed as

$$\underbrace{\frac{\partial}{\partial t} R_k C_k + \frac{\partial}{\partial z} \left(R_k \langle\langle C_k U_{zk} \rangle\rangle \right)}_{\text{(A)}} = \underbrace{-\frac{\partial}{\partial z} \left(R_k \langle\langle \overline{J_k} + \overline{c'_k u'_k} \rangle\rangle \right)}_{\text{(B)}} \tag{59}$$

The term (A), which can be developed as $U_{kz} = \langle\langle U_{kz} \rangle\rangle + \tilde{U}_{kz}$ and $C_k = \langle\langle C_k \rangle\rangle + \tilde{C}_k$, becomes

$$\frac{\partial}{\partial z} \left(R_k \langle\langle C_k U_{kz} \rangle\rangle \right) = \frac{\partial}{\partial z} \left(R_k \langle\langle C_k \rangle\rangle \langle\langle U_{kz} \rangle\rangle \right) + \frac{\partial}{\partial z} \left(R_k \langle\langle \tilde{C}_k \tilde{U}_{kz} \rangle\rangle \right) \tag{60}$$

This term expresses the spatial dispersion and can be modeled as

$$\langle\langle \tilde{C}_k \tilde{U}_{kz} \rangle\rangle = -D_{dk} \frac{\partial \langle\langle C_k \rangle\rangle}{\partial z} \tag{61}$$

Table 5. Experimental and Numerical Values of $E = C/C_0$ at Different Circulation Times

	θ			
	1	2	3	4
E, experimental	1.52	1.12	1.04	1.01
E, 2D	2.26	1.52	1.24	1.10
E, 3D	1.9	1.25	1.08	1.02

Table 6. Numerical Diffusion Coefficient According to Mesh Size

Mesh Size (cm)	D_n (m^2/s)
0.5	4×10^{-4}
1	6.3×10^{-4}
2	1.1×10^{-3}

The term (B) is related to molecular and turbulence diffusion of the concentration:

$$-\frac{\partial}{\partial z}\left(R_k\langle\langle\overline{J_k}+\overline{c_k'u_k'}\rangle\rangle\right)=\frac{\partial}{\partial z}\left\{R_k\left[(D_k+D_{tk})\frac{\partial\langle\langle C_k\rangle\rangle}{\partial z}\right]\right\} \tag{62}$$

referring to the Fickian model and to the concept of turbulent diffusivity.

Finally, one obtains

$$\frac{\partial}{\partial t}R_k\langle\langle C_k\rangle\rangle+\frac{\partial}{\partial z}\left(R_k\langle\langle C_k\rangle\rangle\langle\langle U_{zk}\rangle\rangle\right)=\frac{\partial}{\partial z}\left[R_k(D_k+D_{tk}+D_{dk})\frac{\partial\langle\langle C_k\rangle\rangle}{\partial z}\right] \tag{63}$$

For the sake of simplicity, $\langle\langle F_k\rangle\rangle$ will be noted F_k.

In the case of steady state and fully developed flow, it becomes

$$\frac{\partial R_L}{\partial t}=0 \quad \frac{\partial R_L}{\partial z}=0 \quad \frac{\partial U_L}{\partial z}=0 \quad \frac{\partial D}{\partial z}=0$$

and the transport equation of the concentration becomes

$$\frac{\partial C_L}{\partial t}+U_L\frac{\partial C_L}{\partial z}=(D_L+D_{tL}+D_{dL})\frac{\partial^2 C_L}{\partial z^2} \tag{64}$$

Thus, this equation can be compared to the global equation classically used in tracer method analysis:

$$\frac{\partial C_L}{\partial t}+U_L\frac{\partial C_L}{\partial z}=E_{ZL}\frac{\partial^2 C_L}{\partial z^2} \tag{65}$$

Indeed, with respect to axial dispersion, it is important to define and to estimate the respective weights of the different phenomena that can contribute to it. As written here

$$E_{ZL}=D_L+D_{tL}+D_{dL}+D_{nL} \tag{66}$$

axial dispersion results from molecular diffusion, turbulent diffusion, spatial dispersion, and numerical diffusion. The molecular diffusion of salt in water is about 1.35×10^{-9} m^2/s.

Estimation of numerical and turbulent diffusion and spatial dispersion

Numerical Diffusion. The numerical dispersion is investigated in terms of mesh size and is attributed to the discretization of the transport equation. To calculate its value, a 2D rectangular column (1 m high and 0.1 m wide) is used. At the bottom, a Dirac impulsion is imposed in the domain and the numerical tracer is followed at two points at two different heights (0.4 and 0.8 m). In this case, the dispersion is ensured by only the molecular and numerical diffusions. To reach only the numerical dispersion, different small values of "molecular" diffusion are imposed, that is, between 10^{-2} and 10^{-8} m^2/s. As soon as the solution varies with the fictive molecular diffusion value, it means that dispersion is attributed to numerical diffusion. Because the numerical diffusion depends on mesh size, three squared mesh size were tested: 0.5, 1, and 2 cm.

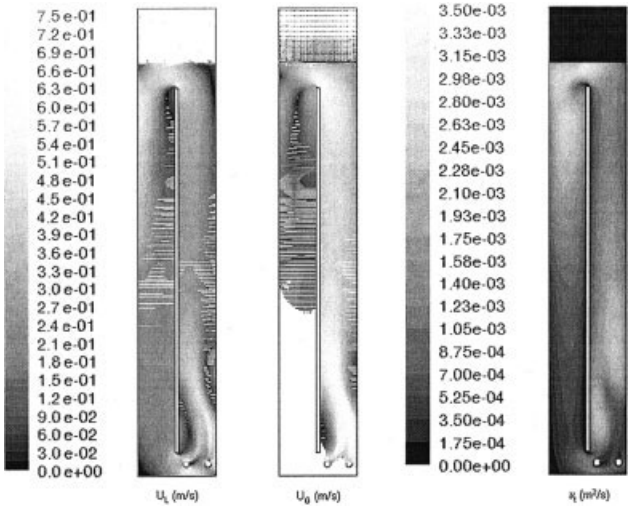

Figure 12. Liquid (U_L), gas velocity (U_G), and liquid turbulent viscosity (v_t).

Table 6 presents the different values of the numerical diffusion coefficient. According to Table 6, the value of D_n varies between 4 and 11 $\times$ 10^{-4} m^2/s. Such values are far greater than the real molecular diffusion ($= 10^{-9}$ m^2/s) but two orders of magnitude smaller than the axial dispersion measured in 2D. Thus, the contribution of numerical diffusion to axial dispersion can be neglected.

Turbulent Dispersion. The second term to estimate is the turbulent diffusivity. As mentioned earlier, it is almost equal to the turbulent viscosity. The turbulent viscosity is plotted

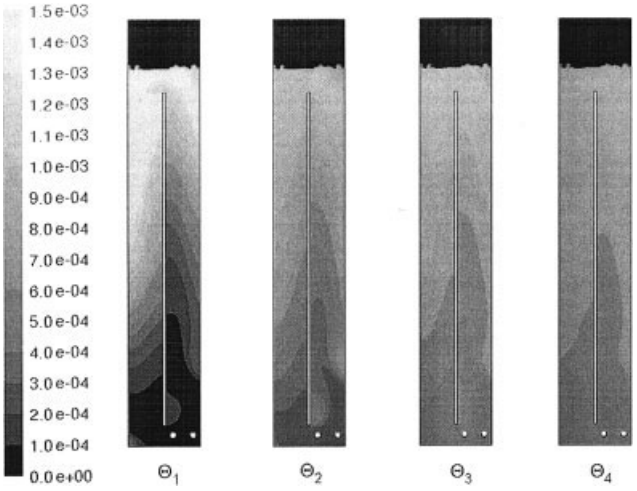

Figure 13. Distribution of concentration after one (Θ_1), two (Θ_2), three (Θ_3), and four (Θ_4) loops.

in Figure 12. The maximum value is 3.5×10^{-3} m^2/s. The averaged value of turbulent viscosity, predicted by the simulation, is 1.8×10^{-3} m^2/s. Surprisingly, it is one order of magnitude smaller than the axial dispersion. Thus, it cannot explain the value of axial dispersion.

Spatial Dispersion. The last term to analyze is the spatial dispersion coefficient. To estimate the longitudinal distribution of spatial dispersion from the simulations, both local liquid velocity and local concentration were decomposed in the cross section, in terms of spatial averaged value and local fluctuation compared to the average as follows:

$$U_L = \langle\langle U_L \rangle\rangle + \tilde{U}_L \qquad \text{and} \qquad C_L = \langle\langle C_L \rangle\rangle + \tilde{C}_L \tag{67}$$

The steady-state liquid velocity field is plotted in Figure 12. The tracer concentration is plotted at different circulation times in Figure 13. As previously demonstrated in the derivation of the one-dimensional equation of the transport of concentration, an additional term accounting for the longitudinal derivative of the correlation $\langle\langle \tilde{C}_L \tilde{U}_L \rangle\rangle$ is introduced. This term accounts for spatial dispersion in the cross section:

$$\langle\langle \tilde{C}_L \tilde{U}_L \rangle\rangle = \frac{\langle \alpha_L \tilde{C}_L \tilde{U}_L \rangle}{R_L} \tag{68}$$

The longitudinal distribution of this term was estimated in the riser and in the downcomer (Figures 14a and 14b). The correlation $\langle\langle \tilde{C}_L \tilde{U}_L \rangle\rangle$ is generally modeled as the product of a spatial dispersion coefficient times the longitudinal gradient of averaged concentration:

$$-\langle\langle \tilde{C}_L \tilde{U}_L \rangle\rangle = D_{dL} \frac{\partial \langle\langle C_L \rangle\rangle}{\partial z}$$

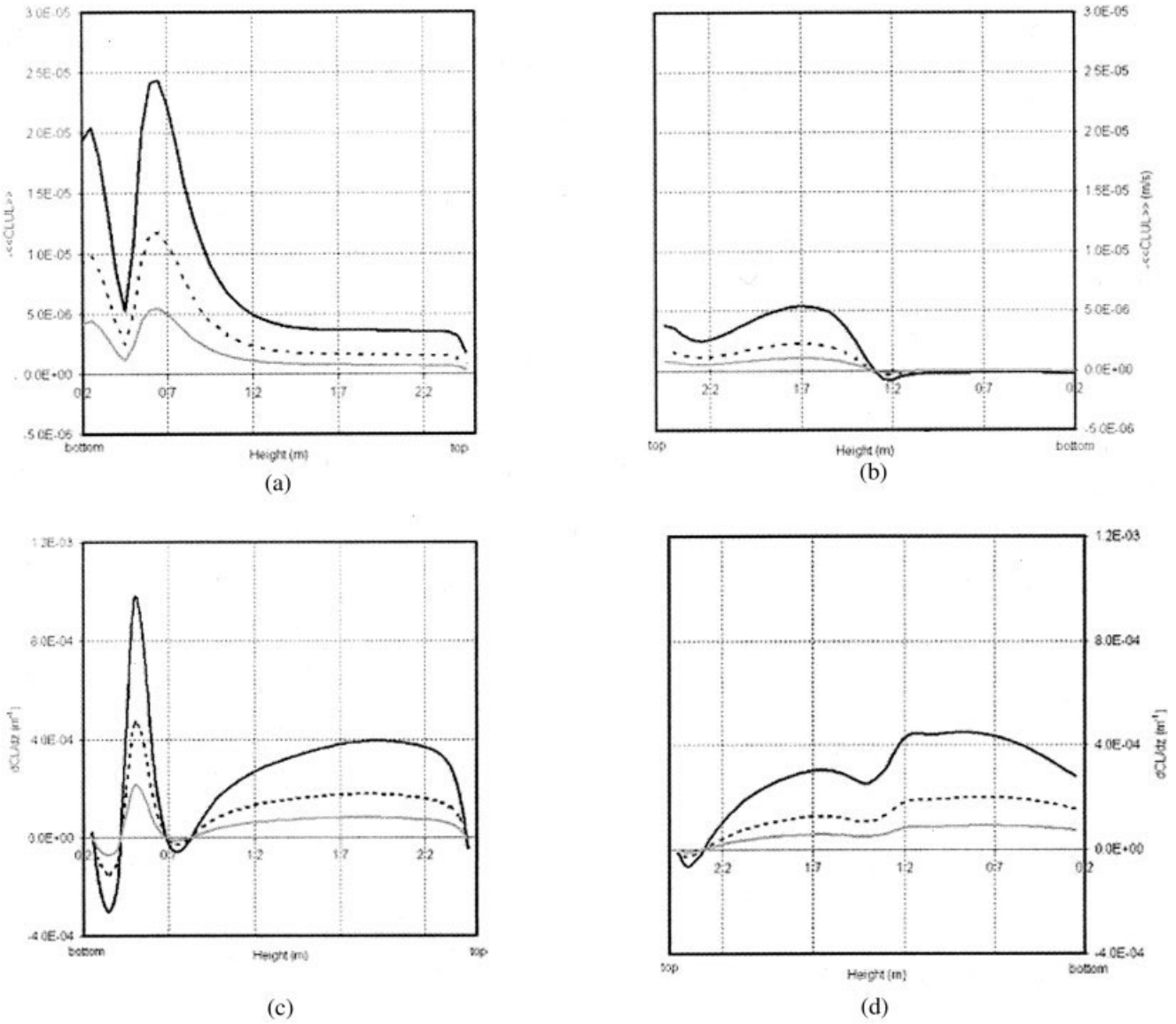

Figure 14. Numerical distribution of $-\langle\langle \tilde{C}_L \tilde{U}_L \rangle\rangle$ in riser (a) and downcomer (b). Numerical distribution of $\partial C_L/\partial z$ in riser (c) and downcomer (d); numerical distribution of D_{dl} in riser (e) and downcomer (f) after two (—: Θ_2), three (- - -: Θ_3), and four (—: Θ_4) loops.

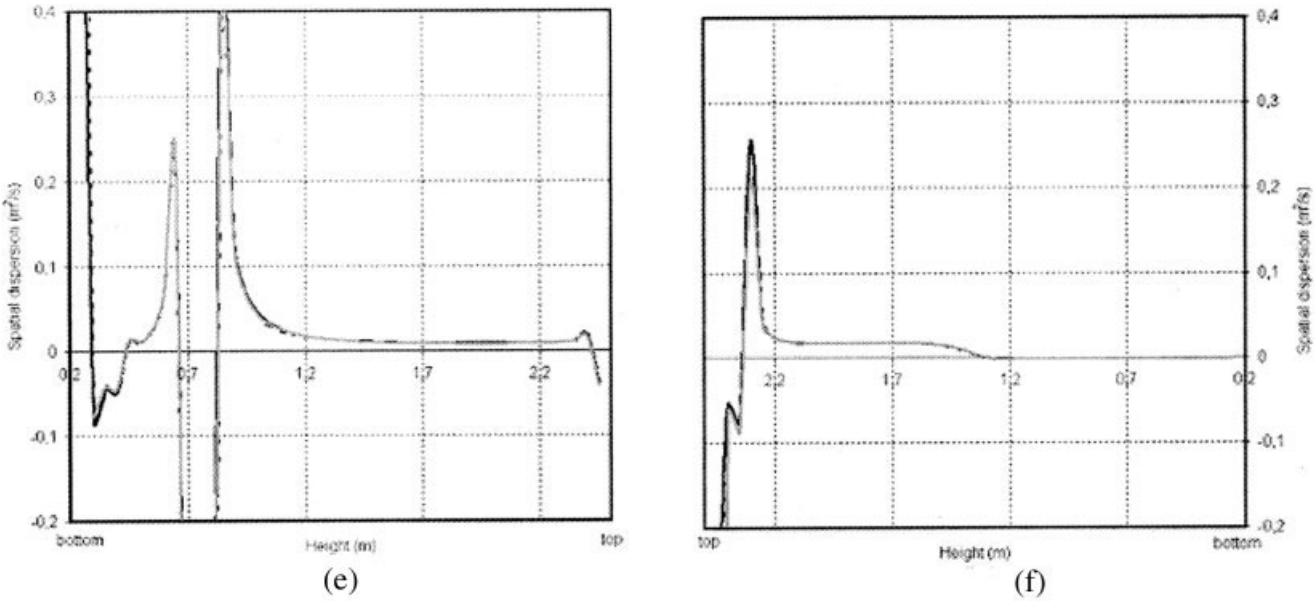

Figure 14. (Continued)

Longitudinal distributions of the longitudinal gradient of averaged concentration $\partial\langle\langle C_L\rangle\rangle/\partial z$ in the riser and in the downcomer were estimated from the simulations and are plotted in Figures 14c and 14d. Three curves are plotted on each figure, corresponding to instantaneous data taken after two, three, and four loops after the injection of salt at the top of the reactor.

It can be noticed that in the riser (Figures 14a–14c), two zones can be characterized, below (Zone 1) and above 1 m high (Zone 2). Zone 1 is the zone where the liquid flow is disturbed by the gas injector and the reversal flow from the downcomer to the riser (Figure 12). The concentration (Figure 13) is trapped in the two recirculation cells in this zone leading to $\partial C_L/\partial z = 0$. In Zone 2, the scalar gradient is almost uniform. The value of $\partial C_L/\partial z$ decreases as the time increases and the concentration becomes uniform throughout the airlift. In the downcomer, two zones can also be described: <1.25 m (Zone 1) and >1.25 m high (Zone 2). Zone 1 is the nonaerated zone of the downcomer. The flow is established and the gradient concentration tends to become uniform according to time. In Zone 2, at the beginning, the concentration is not uniform because the scalar is introduced in this zone. The evolution of $\partial C_L/\partial z$ in the downcomer is similar to the evolution in the riser.

Consequently, the spatial dispersion is defined as follows:

$$D_{dL} = \frac{-\langle\langle \tilde{C}_L \tilde{U}_L\rangle\rangle}{\partial\langle\langle C_L\rangle\rangle/\partial z} \tag{69}$$

and can be estimated after the numerical results.

Figures 14e and 14f show the distribution of the spatial dispersion coefficient in the riser and the downcomer. The first remark is that the three profiles do superimpose, according to Θ_i in the riser as well as in the downcomer. In the riser, D_{dL} in Zone 1 is quite difficult to estimate because $\partial C_L/\partial z$ (Figure 14c) is sometime equal to zero, leading to an infinite value of the spatial dispersion. In Zone 2, D_{dL} is constant and equal in average to 10^{-2} m^2/s. In the downcomer, in Zone 2, D_{dL} is also constant, except at the top where its value is higher because of the acceleration of the liquid velocit. D_{dL} is about 2×10^{-2} m^2/s. In Zone 1 (nonaerated), D_{dL} is also constant and equal to 5×10^{-4} m^2/s. In average, D_{dL} can be estimated as $1.5–2 \times 10^{-2}$ m^2/s in the whole reactor. This value is one order of magnitude higher than the value of the turbulent dispersion v_t (Figure 13).

Clearly, the spatial dispersion is more important than the turbulent diffusion and both molecular and numerical diffusions can be neglected. Because of the strong effect of the complex geometry on spatial dispersion, it becomes clear that the simplification consisting in limiting the simulation to a 2D geometry affects the results: the spatial dispersion induced by the confinement in the third direction has to be taken into account.

3D Simulation. The spatial dispersion coefficient defined by Eq. 69 can also be estimated from profiles of liquid velocity and concentration, at given instants for a 3D simulation. The longitudinal distributions of the spatial dispersion coefficient in the riser and in the downcomer can thus be plotted (Figure 15).

One of the main results observed on Figures 15a and 15b is that the three curves (taken after two, three, and four loops in the airlift) are again superimposed, as in 2D simulation. The second information is related to the nonuniformity of the spatial dispersion coefficient. To better understand this trend, the spatial dispersion coefficient must be differently estimated. In the riser, the velocity field contains positive and negative values, corresponding to a main upflow, in the bulk, and a peripheral downward flow. To be more coherent with the basis of axial dispersion analysis, the spatial dispersion coefficient is now assessed in the restricted upward flow region in the riser and in the restricted downward flow region in the downcomer. The modified spatial dispersion coefficients are plotted in Figures 15c and 15d. These new spatial dispersion coefficients are still nonuniform. Referring to the pioneering works of Taylor,[30] so as to better understand this trend, the spatial dispersion coefficient is usually related to a scale velocity times a length scale. Thus, the longitudinal profile of the average value

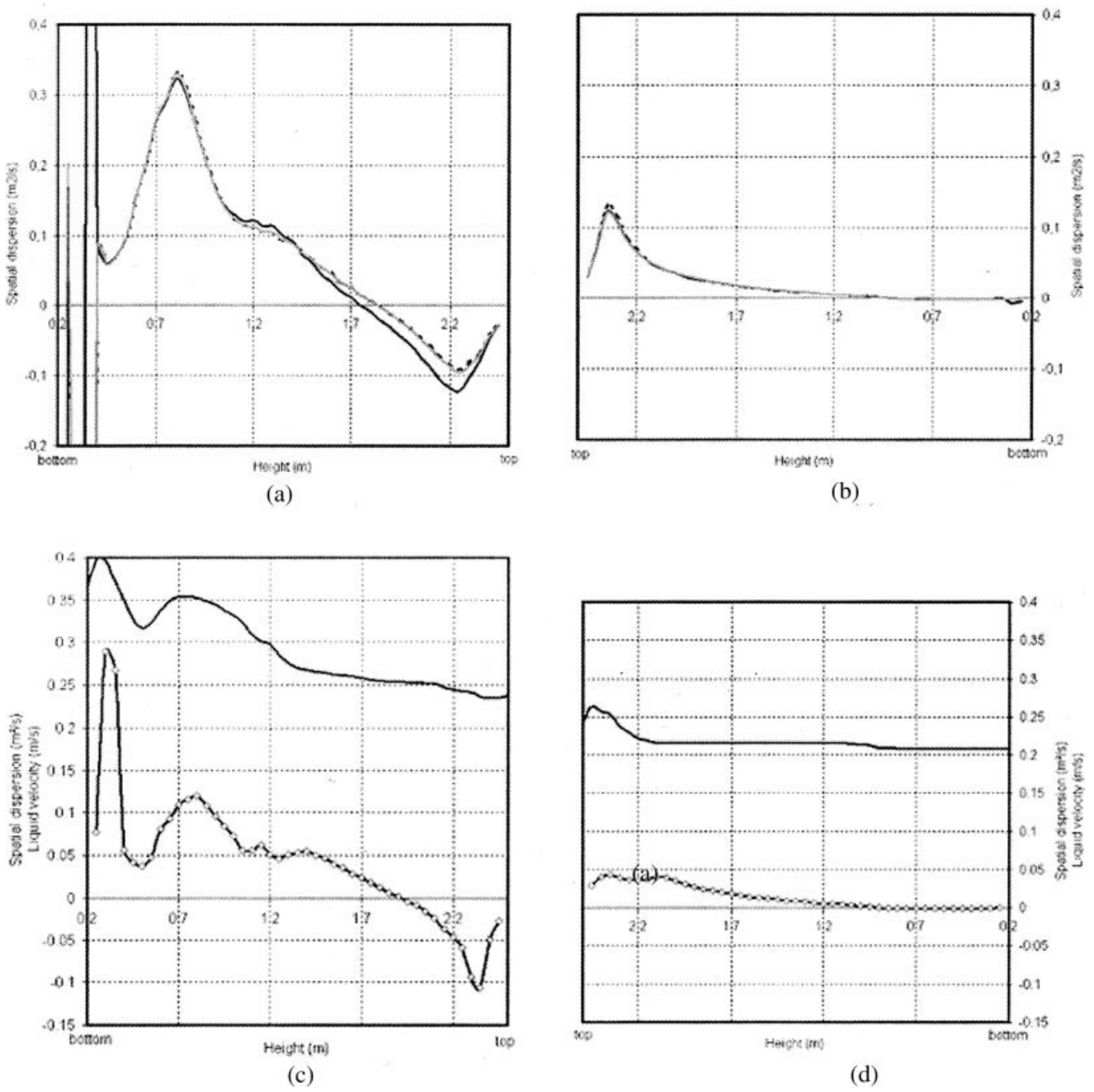

Figure 15. Numerical distribution of spatial dispersion coefficient in riser (a) and downcomer (b) after two (—: Θ_2), three (- - -: Θ_3), and four (——: Θ_4) loops; numerical distribution of modified spatial dispersion coefficient (–◇–) and liquid velocity (—) in riser (c) and downcomer (d).

of the positive (respectively negative) liquid velocity in the riser (respectively in the downcomer) is plotted in Figures 15c and 15d. One can conclude that the longitudinal evolution of the spatial dispersion coefficient in the riser and in the downcomer follows closely the longitudinal evolution of absolute value of the average liquid velocity. In the downcomer, the velocity amplitude is of the order of the liquid circulation, meaning that the downward flow fills the downcomer section, whereas in the riser, in which the velocity amplitude is twice the liquid circulation, a significant downflow occurs along the lateral walls, as in bubble columns. The averaged value of D_{dL} in the riser (respectively downcomer) is 7×10^{-2} m^2/s (respectively 2×10^{-2} m^2/s), leading to a global value $\cong 4.5 \times 10^{-2}$ m^2/s, which is close to the experimental E_{ZL}. Numerical simulations made in 3D are thus more reliable for calculation of axial dispersion. It means that in such an airlift reactor, the complex geometry must be accounted for.

Conclusion on axial dispersion of a tracer in the liquid phase

The main result of the discussion on axial dispersion coefficient is that the turbulent diffusion is shown not to be the

relevant phenomenon able to explain the magnitude of axial dispersion. The spatial dispersion, induced by the complex 3D geometry of the reactor, is shown to be dominant. This result is original, compared to that of previous reports in the literature.[31,32] The evolution of the axial dispersion is also shown to follow the mean liquid velocity. The downcomer behaves like a plug-flow reactor (with weak axial dispersion), whereas the riser behaves in a more complex way, with an axial upflow in the bulk and a recirculating downflow near the wall. From a global perspective, the value of the global axial dispersion coefficient obtained after experiment ($E_{ZL} = 0.04$ m^2/s, Table 4) is of the order of the product of the liquid circulation ($U_L = 0.20$ m/s) times the hydraulic diameter of the airlift ($D_H = 0.3$ m).

Conclusion

Herein we report the most recent attempt to exploit computational fluid dynamics in two-phase flow reactors to predict phase distribution (interfacial area), liquid circulation, and global parameters classically used in chemical engineering such as axial dispersion—the focus has been on an airlift internal loop reactor.

From the simulation of the local hydrodynamics, one can predict the longitudinal distribution of the gas retention and deduce the interfacial area. It must be pointed out that the diameter of the bubble is not modeled but imposed after experimental data. The hydrodynamics has been validated in terms of the liquid velocity profile in the nonaerated part of the downcomer; it was also validated on the longitudinal distribution of gas volume fraction. A sensitivity analysis of the simulations to the main phenomenological relations was investigated. Gas dispersion is mainly related to the modeling of the drift velocity, which is thus a key parameter of the model. The modeling of the drift velocity affects the horizontal velocity of the bubbles, in terms of gas dispersion, and thus gas distribution in the riser and in the downcomer. It does not affect the liquid circulation. Drag coefficient was also shown to be an important issue. The liquid velocity is directly related to the bubble velocity and thus to the modeling of the drag. The gas fraction is also sensitive to the drag modeling. Modeling of free surface deformation can also improve the predictions. With respect to hydrodynamics, 2D simulations seem sufficient to predict gas fraction and liquid circulation.

Given the local hydrodynamics, transport of concentration is simulated. The simulation is compared to experiments in terms of the Voncken model, to determine axial dispersion of a tracer in the liquid phase. The numerical simulation in three dimensions is shown to improve the prediction of this parameter, compared to 2D simulations. It must be mentioned that the turbulent diffusion is one order of magnitude smaller than axial dispersion of a tracer in the liquid phase: the most important phenomenon to explain axial dispersion of a tracer is related to spatial dispersion in the liquid phase, mainly induced by the complex 3D geometry of the airlift internal loop reactor.

The mixing of the liquid phase in the airlift is thus mainly controlled by macroscale effects (velocity scale as liquid circulation and length scale as Taylor macroscale, proportional to the hydraulic diameter); axial dispersion in the liquid phase arises mainly from nonuniform profiles in a section and can be modeled in terms of previous macroscales. The study confirms that the airlift reactor is well adapted to biological processes, with reduced turbulence stresses, but good mixing in terms of macromixing time compared to biological kinetics.

Acknowledgments

The financial support provided by grants from Fonds Social Européen and MESR (Ministère de l'Enseignement Supérieur et de la Recherche) is gratefully acknowledged.

Notation

a_p = projected interfacial area, m^2
B_k = gravitational acceleration, m s^{-2}
C_A = added mass coefficient
C_D = drag coefficient
C_0 = completely mixed concentration, mg L^{-1}
C_k = local statistical averaged concentration in phase k, mg L^{-1}
c_k = local instantaneous concentration in phase k, mg L^{-1}
c'_k = local instantaneous turbulent component of concentration in phase k, mg L^{-1}
$\langle C_L \rangle$ = cross-section–averaged concentration in phase k, mg L^{-1}
$\tilde{C}_L$ = spatial fluctuation of concentration in phase k, mg L^{-1}
$c'u_k$ = turbulent diffusive flux of concentration vector, mg m L^{-1} s^{-1}
d_b = bubble diameter, m
D_L = liquid molecular diffusivity, m^2 s^{-1}
D_{tL} = liquid turbulent diffusivity, m^2 s^{-1}
D_{dL} = liquid dispersion diffusivity, m^2 s^{-1}
D_{dL} = liquid numerical diffusivity, m^2 s^{-1}
$D_{GL}{}^t$ = fluid-bubble turbulent dispersion, m^2 s^{-1}
E = bubble eccentricity
E = concentration ratio
Eö = Eötvös number
E_{ZL} = axial dispersion, m s^{-2}
H = height of the internal wall in the airlift reactor, m
I_k = interfacial transfer of momentum, kg m^{-2} s^{-2}
j_k = superficial phase velocity, m s^{-1}
K = singular head loss coefficient
k_L = turbulent kinetic energy (TKE), m^{-2} s^{-2}
L = length of a liquid circulation loop in the airlift reactor, m
L_k = interfacial transfer of concentration between the two phases, mg L^{-1} s^{-1}
m_k = local instantaneous interfacial mass transfer, kg m^{-3} s^{-1}
M_k = local instantaneous interfacial momentum transfer, kg m^{-2} s^{-2}
M_L = local instantaneous interfacial momentum transfer related to drag, kg m^{-2} s^{-2}
P_k = local statistical averaged phase pressure, kg m^{-1} s^{-2}
ΔP = singular pressure drops, kg m^{-1} s^{-2}
P_w = wall wetted perimeter, m
Pe = Peclet number (Pe $= V_c L/E_{ZL}$)
R_K = volume averaged phase fraction
Re = Reynolds number
r_b = bubble radius, m
S_u = upflow cross-sectional area, m^2
S_d = downflow cross-sectional area, m^2
Sc_t = turbulent Schmidt number
t = time, s
t_c = liquid circulation time, s
U_k = local statistical averaged phase velocity, m s^{-1}
U_r = gas–liquid relative velocity, m s^{-1}
u_k = local instantaneous phase velocity, m s^{-1}
u'_k = local instantaneous turbulent component of phase velocity, m s^{-1}
$\langle U_L \rangle$ = cross-section–averaged phase velocity, m s^{-1}
$\tilde{U}_L$ = spatial fluctuation of phase velocity, m s^{-1}
$u'_k u'_k$ = phasic Reynolds stress tensor, m^2 s^{-2}
V_r = relative velocity, m s^{-1}
v_d = drift velocity, m s^{-1}

Greek letters

α_k = phase retention
δ_i = Dirac function defined at interface locations

ε_L = dissipation rate of the TKE, $m^2\ s^{-3}$
Λ_L = Taylor macroscale of the turbulence in the liquid phase, m
ρ_k = phase density, kg m^{-3}
θ = nondimensional temporal variable ($\theta = t/t_c$)
τ_k = viscous stress tensor in phase k, kg $m^{-1}\ s^{-2}$
τ^t_{GL} = characteristic timescale of the turbulence seen by the gas phase, s
ν_{tL} = turbulent viscosity, $m^2\ s^{-1}$
ζ_r = ratio of the characteristic time of the turbulence in the liquid and the characteristic timescale of the bubble necessary to cross the containing energy eddies
η_r = ratio of the characteristic timescale of the turbulence seen by the gas phase, denoted τ^t_{GL} and the characteristic timescale of the bubble entrainment by the liquid motion τ^F_{GL}

Literature Cited

1. Chisti Y. *Airlift Bioreactors*. New York: Elsevier Applied Science; 1989.
2. Merchuk JC, Gluz M. Fermentation, biocatalysis, bioseparation. In: Ficklinger MC, Stephen WD, eds. *Encyclopedia of Bioprocess Technology*. New York: John Wiley & Sons; 1999;1:320–353.
3. Petersen EE, Margaratis A. Hydrodynamics and mass transfer characteristics of three phase gas–liquid bioreactor systems. *Crit Rev Biotechnol*. 2001;21:233–294.
4. Merchuk JC. Airlift bioreactors: Review of recent advances. *Can J Chem Eng*. 2003;81:324–337.
5. Cockx A, Liné A, Roustan M, Doquang Z, Lazarova V. Numerical simulation and physical modelling of the hydrodynamics in an airlift internal loop reactor. *Chem Eng Sci*. 1997;52:3787–3793.
6. Mudde RF, van den Akker HEA. 2D and 3D simulations of an internal airlift loop reactor on the basis of a two-fluid model. *Chem Eng Sci*. 2001;56:6351–6358.
7. van Baten JM, Ellenger J, Krishna R. Using CFD to describe the hydrodynamics of internal airlift reactors. *Can J Chem Eng*. 2003;81: 660–668.
8. Oey RS, Mudde RF, van den Akker HEA. Numerical simulations of an oscillating internal-loop airlift reactor. *Can J Chem Eng*. 2003;81: 684–691.
9. Clift R, Grace JR, Weber ME. *Bubbles, Drops, and Particles*. San Diego, CA: Academic Press; 1978.
10. Schiller L, Naumann Z. A Drag coefficient correlation. *Z Ver Deutsch Ing*. 1938:77–318.
11. Leon Bécerril E, Liné A. Stability analysis in bubble column. *Chem Eng Sci*. 2001;56:6135–6141.
12. Leon Bécerril E, Liné A. Effect of bubble deformation on stability and mixing in bubble column. *Chem Eng Sci*. 2002;57:3283–3297.
13. Couvert A. *Etude d'un réacteur airlift rectangulaire à recirculation interne*. PhD Thesis. Toulouse, France: INSA; 2000.
14. Cockx A. *Modélisation de contacteurs gaz–liquide: Application de la mécanique des fluides numérique aux airlifts*. PhD Thesis. Toulouse, France: INSA; 1997.
15. van Baten JM, Krishna R. Eulerian simulations for determination of the axial dispersion of liquid and gas phases in bubble columns operating in the churn-turbulent regime. *Chem Eng Sci*. 2001;56: 503–512.
16. Merchuk JC, Contreras A, Garcia F, Molina E. Studies of mixing in a concentric tube airlift bioreactor with different spargers. *Chem Eng Sci*. 1998;53/54:709–719.
17. Mudde RF, Simonin O. 2D and 3D simulations of a bubble plume using a two-fluid model. *Chem Eng Sci*. 1999;54:5061–5069.
18. Bel F'Dhila R, Simonin O. Eulerian prediction of a turbulent bubbly flow down-stream a sudden pipe extension. Proceedings of the Sixth Workshop on Two Phase Flow Predictions, Erlangen, Germany; 1992.
19. Karamanev DG, Nikolov LN. Free rising spheres do not obey Newton's laws for free settling. *AIChE J*. 1992;38:1843–1846.
20. Simonin O, Viollet PL. Modelling of turbulent two-phase jets loaded with discrete particles. In: Hewitt G, Mayinger F, Riznic JR, eds. *Phase Interface Phenomena in Multiphase Flow*. Washington, DC: Hemisphere; 1990:259–270.
21. Haynes PA. *Contribution à la modélisation de la turbulence pour les écoulements à bulles: Proposition d'un modèle (k–ε) multi-échelles diphasique*. PhD Thesis. Toulouse, France: INP; 2004.
22. Elghobashi SE, Abou-Arab TW. A two-equation turbulence model for two-phase flow. *Phys Fluids*. 1983;26:931.
23. Couvert A, Roustan M, Chatellier P. Two-phase hydrodynamic study of a rectangular air-lift loop reactor with an internal baffle. *Chem Eng Sci*. 1999;54:5245–5252.
24. Couvert A, Bastoul D, Roustan M, Chatellier P. Hydrodynamic and mass transfer study in a rectangular three-phase air-lift loop reactor. *Chem Eng Process*. 2004;43:1381–1387.
25. Bugay S, Escudié R, Liné A. Experimental analysis of hydrodynamics in axially agitated tank using P.I.V. technique. *AIChE J*. 2002;48: 463–475.
26. Sokolichin A, Eigenberger G, Lapin A, Lübert A. Dynamic numerical simulation of gas–liquid two-phase flows Euler/Euler versus Euler/Lagrange. *Chem Eng Sci*. 1997;52:611–626.
27. Talvy S. *Airlift et Colonne à Bulles en Écoulements Gaz–Liquide et Gaz–Liquide–Solide*. PhD Thesis. Toulouse, France: INSA; 2003.
28. Saez AE, Marquez MA, Roberts GW, Carbonnel RC. Hydrodynamics model for gas-lift reactors. *AIChE J*. 1998;44:1413–1423.
29. Harmathy TJ. Velocity of large drops and bubbles in media of infinite or restricted extent. *AIChE J*. 1960;6:281–288.
30. Taylor GI. The dispersion of matter in turbulent flow through a pipe. *Proc R Soc Lond A Phys Sci*. 1954;A223:446.
31. Joshi JB, Ranade VV, Gharat SD, Lele SS. Sparged loop reactors. *Can J Chem Eng*. 1990;68:705–741.
32. Vial C, Poncin S, Wild G, Midoux N. Experimental and theoretical analysis of axial dispersion in the liquid phase in external-loop airlift reactors. *Chem Eng Sci*. 2005;60:5945–5954.

Manuscript received July 7, 2006, and revision received Oct. 24, 2006.